Article

Cell Reports

Methylglyoxal Scavengers Resensitize KRAS-Mutated Colorectal Tumors to Cetuximab

Graphical Abstract

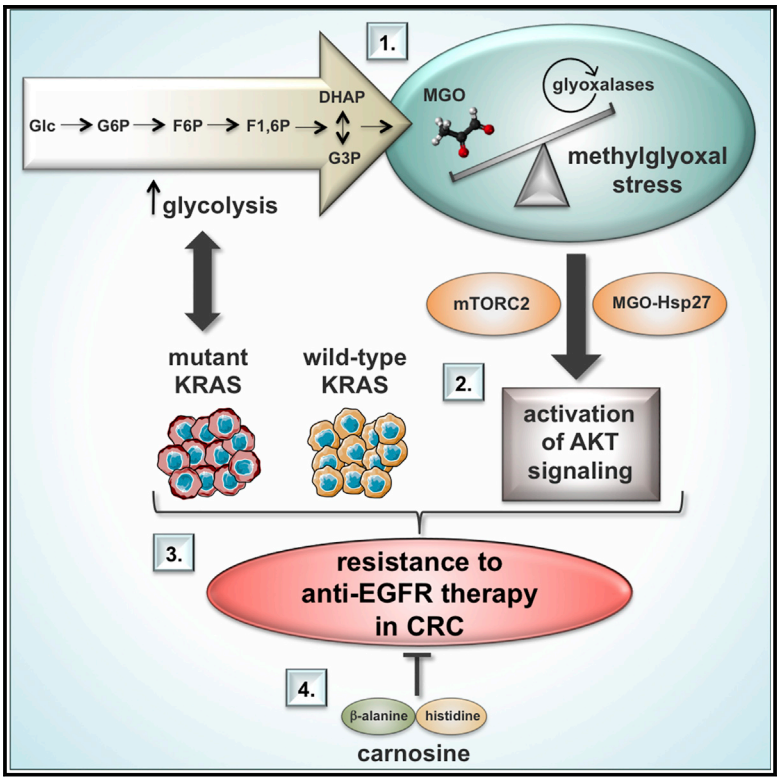

Highlights

- Glycolytic mutant KRAS display higher MGO stress than wild-type CRC cells
- MGO stress is a potent inducer of AKT signaling in CRC cells
- MGO stress induces resistance to anti-EGFR therapy in a wild-type KRAS setting
- Carnosine, an MGO scavenger, sensitizes mutant KRAS CRC tumors to anti-EGFR therapy

Authors

Justine Bellier, Marie-Julie Nokin, Maurine Caprasse, ..., Olivier Peulen, Vincent Castronovo, Akeila Bellahcène

Correspondence

a.bellahcene@uliege.be

In Brief

Bellier et al. demonstrate that MGO stress is a constant feature of KRAS-mutated CRC tumors. MGO induces a key survival pathway implicated in resistance to EGFR-targeted therapy in CRC. The scavenging of this oncometabolite could be beneficial in the treatment of both wild-type and mutant KRAS CRC tumors.

Bellier et al., 2020, Cell Reports *30*, 1400–1416
February 4, 2020
https://doi.org/10.1016/j.celrep.2020.01.012

CellPress

OPEN ACCESS
CellPress

Cell Reports
Article

Methylglyoxal Scavengers Resensitize KRAS-Mutated Colorectal Tumors to Cetuximab

Justine Bellier,[1] Marie-Julie Nokin,[1] Maurine Caprasse,[1] Assia Tiamiou,[1] Arnaud Blomme,[2] Jean L. Scheijen,[3] Benjamin Koopmansch,[4] Gillian M. MacKay,[2] Barbara Chiavarina,[1] Brunella Costanza,[1] Gilles Rademaker,[1] Florence Durieux,[1] Ferman Agirman,[1] Naïma Maloujahmoum,[1] Pino G. Cusumano,[5] Pierre Lovinfosse,[6] Hing Y. Leung,[2,7] Frédéric Lambert,[4] Vincent Bours,[4] Casper G. Schalkwijk,[3] Roland Hustinx,[6] Olivier Peulen,[1] Vincent Castronovo,[1] and Akeila Bellahcène[1,8,*]

[1]Metastasis Research Laboratory, GIGA-Cancer, University of Liège, Liège, Belgium
[2]Cancer Research UK Beatson Institute, Glasgow, United Kingdom
[3]Laboratory for Metabolism and Vascular Medicine, Department of Internal Medicine, Maastricht University, Maastricht, the Netherlands
[4]Department of Human Genetics, Liège University Hospital, Liege, Belgium
[5]Department of Senology, Liège University Hospital, University of Liège, Liège, Belgium
[6]Oncology Imaging Division, Liège University Hospital, University of Liège, Liège, Belgium
[7]Institute of Cancer Sciences, University of Glasgow, Glasgow, United Kingdom
[8]Lead Contact
*Correspondence: a.bellahcene@uliege.be
https://doi.org/10.1016/j.celrep.2020.01.012

SUMMARY

The use of cetuximab anti-epidermal growth factor receptor (anti-EGFR) antibodies has opened the era of targeted and personalized therapy in colorectal cancer (CRC). Poor response rates have been unequivocally shown in mutant KRAS and are even observed in a majority of wild-type KRAS tumors. Therefore, patient selection based on mutational profiling remains problematic. We previously identified methylglyoxal (MGO), a by-product of glycolysis, as a metabolite promoting tumor growth and metastasis. Mutant KRAS cells under MGO stress show AKT-dependent survival when compared with wild-type KRAS isogenic CRC cells. MGO induces AKT activation through phosphatidylinositol 3-kinase (PI3K)/mammalian target of rapamycin 2 (mTORC2) and Hsp27 regulation. Importantly, the sole induction of MGO stress in sensitive wild-type KRAS cells renders them resistant to cetuximab. MGO scavengers inhibit AKT and resensitize KRAS-mutated CRC cells to cetuximab *in vivo*. This study establishes a link between MGO and AKT activation and pinpoints this oncometabolite as a potential target to tackle EGFR-targeted therapy resistance in CRC.

INTRODUCTION

Cancer cells undergo an adaptive metabolic shift, known as the Warburg effect, toward increased use of aerobic glycolysis when compared with normal cells. In addition to produce ATP, the glycolytic pathway provides metabolic intermediates needed for cell growth and proliferation (Vander Heiden and DeBerardinis, 2017). One unavoidable consequence associated with elevated glycolytic flux is the spontaneous formation of methylglyoxal (MGO) from triose phosphate intermediates (Richard, 1993). MGO is a highly reactive dicarbonyl compound that glycates proteins, DNA, and lipids much more efficiently than glucose (Brownlee, 2001; Maessen et al., 2015; Thornalley et al., 1995). MGO post-translational modification of arginine residues notably leads to the formation of argpyrimidine and dihydroxy-imidazolone (MGO-Hs) protein adducts (Rabbani and Thornalley, 2012a). Heat shock proteins are direct targets of MGO glycation, with heat shock protein 27 (Hsp27) being the best-characterized argpyrimidine detected in several cancer types, including human colorectal cancer (CRC). MGO-modified Hsp27 (MGO-Hsp27) is more stable and active than native Hsp27 and favors cancer cell escape from apoptosis (Oya-Ito et al., 2006; Sakamoto et al., 2002; van Heijst et al., 2006).

MGO is efficiently detoxified to D-lactate by glyoxalase 1 (GLO1), an ubiquitous cellular enzyme (Rabbani and Thornalley, 2012b). Using a GLO1-silencing strategy, we previously demonstrated that the direct modification of Hsp90 by MGO favors YAP nuclear localization and the inactivation of the Hippo tumor suppressor pathway in breast cancer cells (Nokin et al., 2016). We showed that MGO stress endowed breast cancer cells with enhanced growth and metastatic potential, both of which were efficiently blocked *in vivo* using MGO scavenger molecules such as carnosine (beta alanyl-L-histidine) and aminoguanidine (Nokin et al., 2016, 2019). MGO is cytotoxic and mutagenic, and several studies demonstrated the pro-apoptotic effect of MGO stress on cancer cells. In fact, we recently contributed to reveal the dual role of MGO stress by demonstrating its hormetic effect on cancer cells, with low concentrations supporting tumor growth and high levels inducing toxicity and apoptotic death (Nokin et al., 2017).

KRAS mutation represents one of the most prevalent genetic alterations in cancers. In CRC tumors, ~85%–90% of *KRAS* mutations occur in exon 2, with codon 12 and 13 being the most predominant mutations. In particular, $KRAS^{G12V}$ mutation is associated with resistance to apoptosis through AKT activation (Alamo et al., 2015; Guerrero et al., 2000), higher metastatic potential (Alamo et al., 2015), and mitochondrial dysfunction leading to glycolytic reprogramming (Hu et al., 2012). Cetuximab anti-epidermal growth factor receptor (anti-EGFR) therapy is

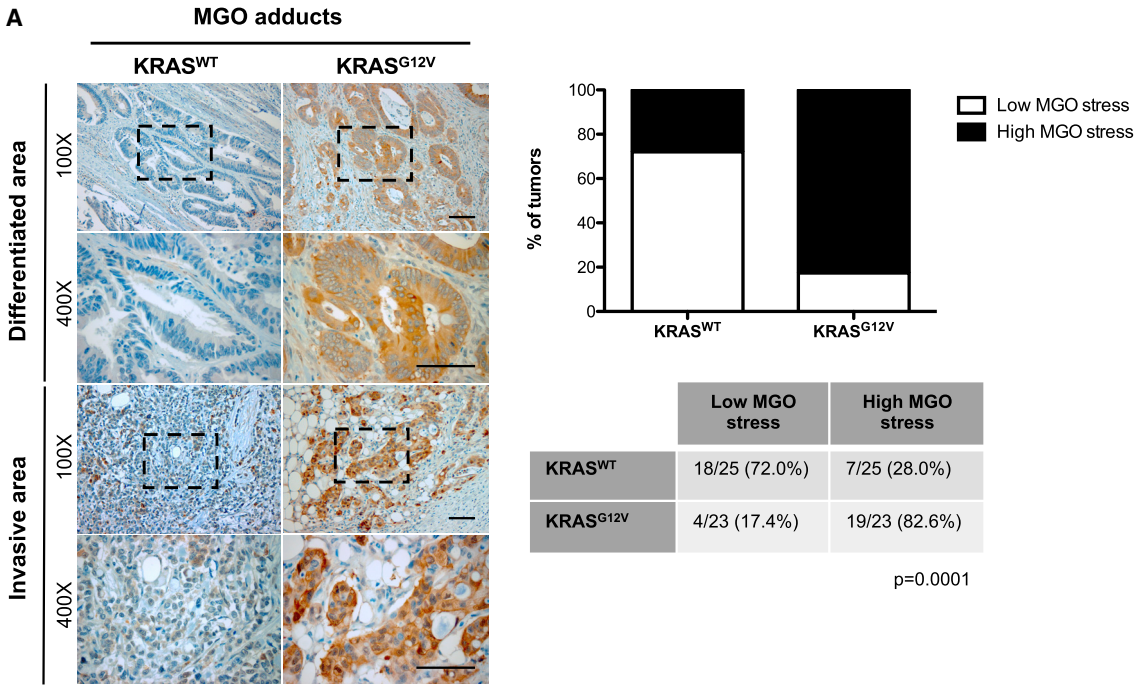

	Low MGO stress	High MGO stress
KRAS^{WT}	18/25 (72.0%)	7/25 (28.0%)
KRAS^{G12V}	4/23 (17.4%)	19/23 (82.6%)

p=0.0001

Figure 1. Evidence of MGO Dicarbonyl Stress in KRAS-Mutated Human CRC Tumors

(A) Detection of MGO adducts as assessed by IHC of argpyrimidines in a series of colon cancer tumors (n = 48). Two representative KRAS^{WT} and KRAS^{G12V} mutated CRC tumors are shown. Data are shown as percentage of tumors presenting MGO stress in KRAS^{WT} and KRAS^{G12V} tumors and were analyzed using a chi-square contingency test (p = 0.0001). The lower images show the area within the dashed rectangle on the upper images at higher magnification. Scale bars represent 100 μm. See also Figure S1.

aimed at the targeting of the two major pathways activated through EGFR. The RAS/RAF/MEK/ERK pathway, which controls gene transcription, cell-cycle progression, and cell proliferation, and the phosphatidylinositol 3-kinase (PI3K)/AKT pathway, which activates a cascade of anti-apoptotic and pro-survival signals. The molecular mechanisms that contribute to the development of primary and secondary resistance to cetuximab in CRC are the subject of intensive clinical and research studies in order to propose new combined modality approaches (Bardelli and Siena, 2010; De Roock et al., 2011; Hong et al., 2016). The detection of KRAS mutation rapidly revealed to be a strong and useful negative predictive biomarker of CRC response to cetuximab (Allegra et al., 2016; Lièvre et al., 2006).

Parallel activation of RAS and PI3K pathways (for review, see Castellano and Downward, 2011) confers maximal resistance to cetuximab (Jhawer et al., 2008) and points to PI3K/AKT activation as a crucial player in CRC resistance to targeted EGFR therapy. Direct interaction of activated KRAS with PI3K subunit p110 (Downward, 2003; Gupta et al., 2007; Rodriguez-Viciana et al., 1994) has been proposed to explain the constitutive activation of the PI3K/AKT pathway in a KRAS-mutated setting and its crucial role in KRAS-mediated transformation. However, it is noteworthy that in CRC, the knockdown of KRAS in mutant cell lines did not suppress AKT phosphorylation and led to the discovery of other dominant mechanisms underlying AKT activation in a KRAS-mutated setting, such as specific tyrosine kinase receptor signaling (i.e., insulin-like growth factor I receptor) (Ebi et al., 2011). A better understanding of how AKT signaling is activated in KRAS mutant CRC will point to potential therapeutic strategies against these tumors refractory to EGFR-targeted therapy.

Our previous demonstration of elevated MGO adducts in human CRC tumors presenting high FDG-PET (fluorodeoxyglucose positron emission tomography) metabolic activity (Chiavarina et al., 2017) and the glycolytic switch shown to occur in KRAS mutant CRC cells (Hu et al., 2012) prompted us to (1) assess endogenous MGO stress in KRAS-mutated tumors and cell lines and (2) envisage the possibility that MGO scavengers could re-sensitize mutant KRAS tumors to cetuximab.

Using two series of human CRC tumors, we found that the majority of KRAS^{G12V} tumors presented high MGO stress and that this latter correlated with the detection of phosphorylated AKT (P-AKT). We used SW48 and LIM1215 isogenic human CRC models, consisting of targeted heterozygous knockin of KRAS^{G12V}, to compare KRAS-mutated cells to their wild-type counterparts (KRAS^{WT}), which do not harbor other frequent CRC oncogenic mutations (i.e., PTEN, NRAS, BRAF, and PIK3CA). Such models elude variability of the genetic background between CRC cell lines that confounds attribution of results directly to the presence of mutant KRAS. We found elevated MGO levels and adducts in KRAS^{G12V} when compared with KRAS^{WT} cells. Exogenous and endogenous (GLO1 silencing) MGO stress induced a significant activation of AKT, in wild-type and mutant KRAS, that was abrogated using MGO scavengers. *In vitro*, the combination of cetuximab and carnosine inhibited KRAS-mutated tumor growth. Importantly, the sole MGO stress induction in cetuximab-sensitive KRAS^{WT}

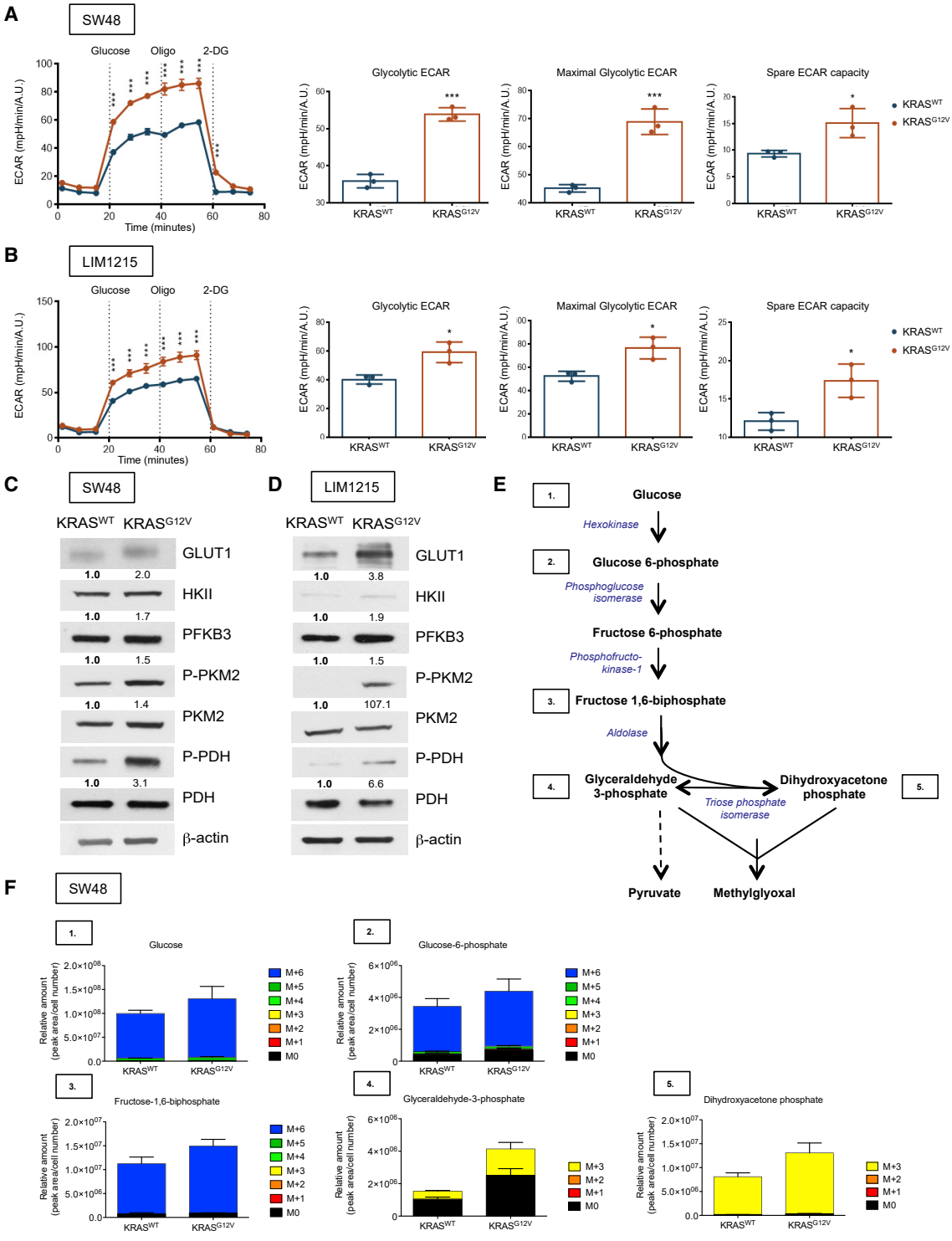

Figure 2. KRAS^{G12V} Cells Are More Glycolytic than Isogenic Wild-Type CRC Cells

(A and B) Kinetic measurement of extracellular acidification rate (ECAR) in SW48 CRC cells (A) and LIM1215 CRC cells (B) in response to glucose (20 mM), oligomycin (oligo, 1 μM), and 2-deoxyglucose (2-DG, 50 mM). Significantly higher glycolytic, maximal, and spare ECAR capacities were observed in KRAS^{G12V} cells when compared with KRAS^{WT} cells. Seahorse data were normalized with cell number evaluated using Hoechst incorporation (arbitrary unit [A.U.]). One representative experiment out of three is shown. Each data point represents mean ± SD, n = 3. ***$p < 0.001$ and *$p < 0.05$.

(legend continued on next page)

CRC cells rendered them resistant. Therefore, MGO stress, which we prove to be implicated in KRAS-mutated resistance, should be also taken into account when predicting the efficacy of EGFR-targeted drugs in a wild-type CRC clinical setting.

RESULTS

Evidence of MGO Dicarbonyl Stress in KRAS-Mutated CRC Human Tumors and Cell Lines

In glycolytic cells, MGO production and the formation of protein adducts generate MGO dicarbonyl stress conditions. We previously demonstrated that elevated MGO adducts are detected in human CRC malignant lesions when compared with matched normal colon and are correlated with a pathological stage (Chiavarina et al., 2017). Using immunohistochemistry (IHC), we specifically evaluated the levels of MGO adducts in $KRAS^{WT}$ and KRAS-mutated ($KRAS^{G12V}$) CRC tumors (n = 48). MGO adducts were mainly detectable in the cytoplasm of cancer cells (Figure 1A). Remarkably, both differentiated and stroma infiltrating tumor cells displayed detectable MGO adducts in $KRAS^{G12V}$ tumors (Figure 1A). The intensity and extent of the immunostaining were scored, and tumor MGO dicarbonyl stress was evaluated as high or low, as detailed in STAR Methods. The majority of $KRAS^{G12V}$ tumors displayed high MGO dicarbonyl stress when compared with $KRAS^{WT}$ tumors (chi-square test, p = 0.0001) (Figure 1A). We observed a similar correlation between KRAS mutation and MGO stress using a series of 84 rectal human tumors (Fisher's test, p = 0.03) that we previously characterized for their KRAS status (Lovinfosse et al., 2016) (Figure S1A).

$KRAS^{G12V}$ Cells Are More Glycolytic than Isogenic Wild-Type CRC Cells

We used SW48 and LIM1215 isogenic CRC models to systematically characterize the effects of KRAS mutation on cell glycolytic phenotype. First, the quantitative measurement of the glycolytic rate of SW48 and LIM1215 cells demonstrated that $KRAS^{G12V}$ cells presented a significantly higher glycolytic capacity upon glucose challenge than $KRAS^{WT}$ cells (Figures 2A and 2B, respectively). Glycolytic, maximal, and spare ECAR (extracellular acidification rate) notably indicated that $KRAS^{G12V}$ rely more on glycolysis than $KRAS^{WT}$ cells in both SW48 and LIM1215 models (Figures 2A and 2B, respectively). Accordingly, GLUT1 glucose transporter expression was significantly elevated in KRAS-mutated cells (Figures 2C and 2D). Second, we evaluated the expression of key glycolysis cascade enzymes in $KRAS^{WT}$ versus $KRAS^{G12V}$ cells. Critical regulatory enzymes in glycolytic control, including hexokinase II (HK II), PFKB3, the active M2 splice variant of pyruvate kinase (P-PKM2), and inactive pyruvate dehydrogenase (P-PDH) presented with higher basal expression levels in $KRAS^{G12V}$ cells than in $KRAS^{WT}$ cells in the SW48 (Figure 2C) and LIM1215 (Figure 2D) models. Third, ^{13}C-labeled glucose flux analysis confirmed enhanced glucose uptake and elevated amounts of the first intermediates of the glycolysis pathway (Figure 2E) in SW48 $KRAS^{G12V}$ cells (Figure 2F). Taken together, these results indicate that $KRAS^{G12V}$ cells present a rewired glucose metabolism promoted by the overexpression of key effectors of the glycolytic pathway. These data and our previous demonstration of MGO adducts accumulation in high ^{18}F-FDG-PET CRC tumors (Chiavarina et al., 2017) urged us to characterize for the first time MGO stress in the context of mutant KRAS CRC cells.

Glycolytic Mutant KRAS Cells Produce Higher Amounts of MGO than Isogenic Wild-Type CRC Cells

In good accordance with their glycolytic phenotype, $KRAS^{G12V}$ SW48 and LIM1215 cells showed a higher level of MGO than $KRAS^{WT}$ cells, as measured in their conditioned media using liquid chromatography-tandem mass spectrometry (LC-MS/MS) (Figure 3A). Using this technique, we also detected ^{13}C-labeled MGO in CRC cells challenged with ^{13}C-glucose, thus providing the first evidence of MGO being a glycolysis by-product detectable in cancer cells and secreted in the medium (Figure 3B). Higher accumulation of MGO adducts (argpyrimidines and MG-Hs) was detected in $KRAS^{G12V}$ SW48 (Figure 3C) and LIM1215 (Figure 3C) cells when compared with $KRAS^{WT}$ isogenic cells. GLO1 expression (Figure 3E), GLO1 enzymatic activity (Figure 3F), and D-lactate production (Figure S2A) were similar in $KRAS^{WT}$ and $KRAS^{G12V}$ settings. Accordingly, exogenous MGO was detoxified into D-lactate by GLO1 with comparable efficiency independently of KRAS status (Figure S2B). Altogether, these data indicate that elevated MGO and MGO adducts levels observed in KRAS-mutated cells are likely related to their favored usage of glycolysis, since their GLO1 detoxification capacity is comparable to the one observed in $KRAS^{WT}$ cells.

MGO Stress Induces AKT Activation in CRC Cells that Is Reverted Using MGO Scavengers

The activation of AKT promotes glucose uptake and stimulates aerobic glycolysis in cancer cells (Elstrom et al., 2004; Rathmell et al., 2003). We next observed that basal levels of P-AKT and its downstream targets, P-GSK3beta and P-P70S6K, were consistently elevated in $KRAS^{G12V}$ cells compared with $KRAS^{WT}$ cells (Figure 4A). To check whether this marked difference in AKT activation could be related to MGO stress conditions, we treated the cells with two potent MGO scavengers. Both carnosine (Figure 4B) and aminoguanidine (Figure 4C) significantly decreased P-AKT levels in both $KRAS^{WT}$ and $KRAS^{G12V}$ cells, thus confirming the implication, at least in part, of MGO stress in the regulation of AKT activity. To support this important observation, we next reasoned that exogenous MGO treatment should induce AKT activation in CRC cells. In isogenic models (Figure 4D), it is remarkable that MGO treatment induced a dose-dependent P-AKT activation

(C and D) GLUT1, HXII, PFKFB3, P-PKM2, PKM2, P-PDH, and PDH levels were assessed in SW48 CRC cells (C) and LIM1215 CRC cells (D) using western blot. A representative western blot of at least two independent experiments is shown. β-Actin was used for normalization.

(E) Schematic representation of the first steps of glycolysis and MGO production.

(F) ^{13}C-glucose metabolic flux analysis performed in SW48 CRC cells using mass spectrometry. Higher glucose and glycolytic intermediates (numbered as in E) were observed in $KRAS^{G12V}$ CRC cells when compared with $KRAS^{WT}$ CRC cells. Data are expressed as peak area/number of cells. Data are shown as mean values ± SEM of three independent experiments.

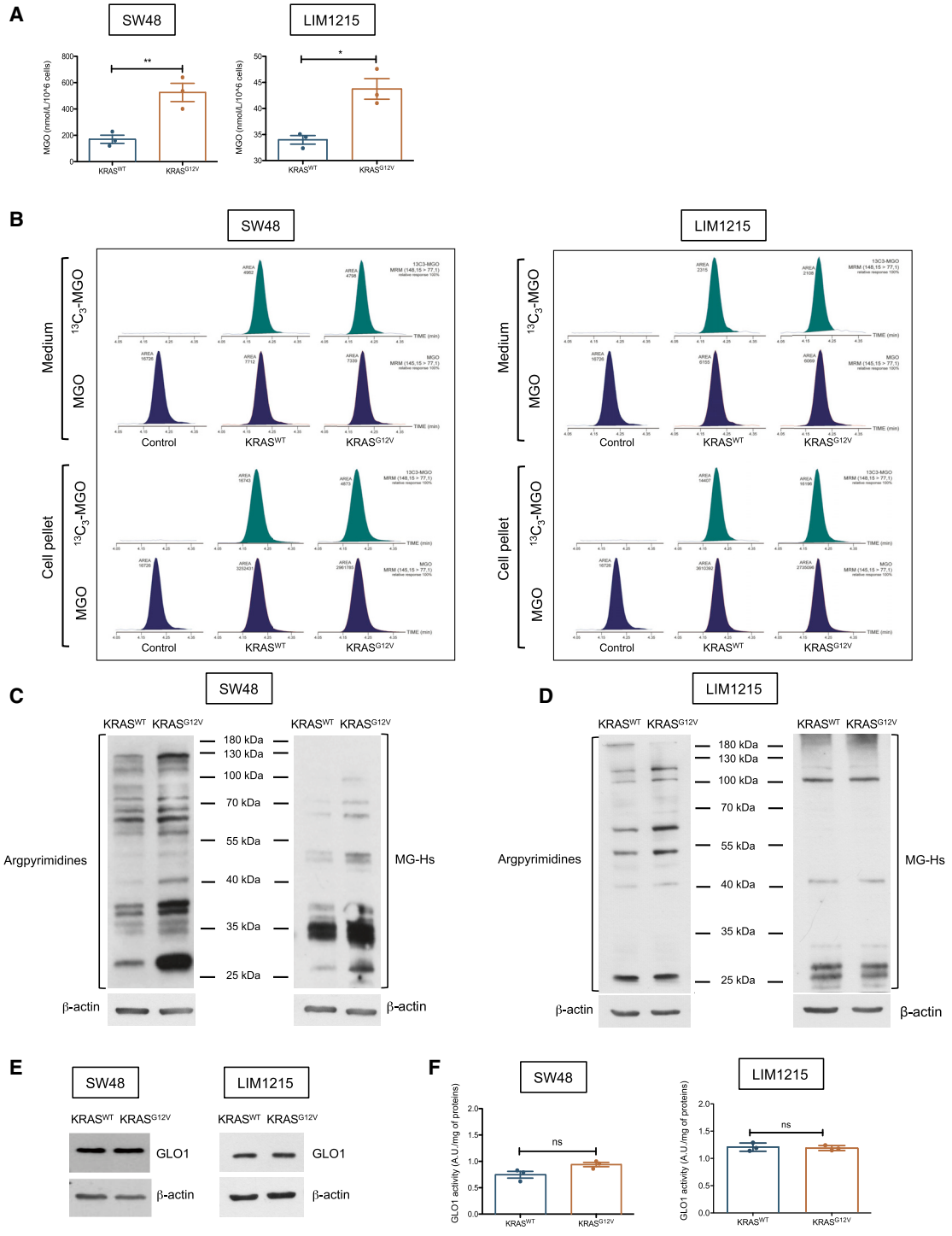

Figure 3. Glycolytic Mutant KRAS Cells Produce Higher Amounts of MGO than Isogenic Wild-Type CRC Cells

(A) MGO quantification in CRC isogenic models using LC-MS/MS analysis on conditioned culture media. Data were analyzed using unpaired Student's t test and are shown as mean values ± SEM of three independent experiments.

(B) Detection of ^{13}C-labeled MGO and unlabeled MGO in CRC cells using LC-MS/MS analysis in conditioned media and cell pellets. Plasma EDTA samples were used as control for MGO detection (control).

(C and D) Western blot detection of MGO adducts (argpyrimidines and MG-Hs) in SW48 cells (C) and LIM1215 CRC cells (D).

(legend continued on next page)

in KRAS^{WT} cells. In KRAS^{G12V} cells, the highest doses of MGO also increased P-AKT level over the high basal levels constantly detected in these cells. Elevated intracellular MGO levels were evidenced upon MGO treatment in CRC cells using methyl diaminobenzene-BODIPY (MBo), a fluorescent sensor of MGO (Wang et al., 2013) (Figure S3A). It is noteworthy that MGO induced significant activation of AKT in a panel of human CRC cell lines (i.e., HT29, SW480, HCT116, and Lovo) (Figure 4E) regardless of their mutational profile (Figure 4F), thus establishing a link between MGO stress and AKT activation. Consistently, we found that a majority of high-P-AKT CRC tumors presented with high MGO stress when compared with low-P-AKT tumors (Fisher's test, $p = 0.03$) (Figure 4G). Remarkably, the sole induction of an endogenous MGO stress through the inhibition of GLO1 expression using specific small interfering RNAs (siRNAs) recapitulated AKT activation in the SW48 isogenic model (Figure 4H). Increased MGO levels were detected in GLO1 silenced SW48 cells when compared with control cells using both the MBo fluorescent sensor of MGO (Figure S3B) and LC-MS/MS (Figure S3C). Sustaining further the relationship between *de novo* MGO stress induction and P-AKT levels is the fact that the co-treatment with MGO and its scavengers, carnosine (Figure 4I) and aminoguanidine (Figure 4J), effectively reversed MGO-mediated AKT activation in CRC cells. The significant decrease of MGO levels was verified in carnosine- and aminoguanidine-treated SW48 cells using LC-MS/MS (Figure S3D).

MGO-Mediated Activation of AKT Occurs through PI3K and mTORC2 in CRC Cells

In order to explore the molecular mechanisms underlying MGO-mediated AKT phosphorylation, we first checked the possibility that MGO could regulate PI3K upstream of AKT activation. We observed that MGO treatment induced the activation of PI3K in KRAS^{WT} CRC cells and KRAS^{G12V} LIM1215 cells (Figure 5A). Next, we focused on the mammalian target of rapamycin 2 (mTORC2), because this complex directly phosphorylates AKT on Ser473 (Sarbassov et al., 2005). We found that MGO treatment was sufficient to induce the expression of the mTORC2 components Rictor and mTOR in KRAS^{WT} CRC cells (Figure 5B). MGO induction of mTORC2 was not significant in KRAS^{G12V} CRC cells (data not shown), possibly because of their high basal level of mTORC2 complex when compared with KRAS^{WT} cells that is likely attributable to the direct binding and activation of mTORC2 by mutated RAS, as reported recently (Kovalski et al., 2019). Importantly, the use of torin 1 (an mTORC1 and mTORC2 inhibitor) completely blocked MGO-mediated AKT activation, while rapamycin (an mTORC1 inhibitor) did not (Figures 5C and 5D) in KRAS^{WT} and KRAS^{G12V} settings in both isogenic models. These data demonstrate that MGO acts as a potent inducer of AKT activation through the PI3K/mTORC2 axis.

High MGO-Glycated Hsp27 (MGO-Hsp27) Sustains AKT Activation in KRAS^{G12V} Cells

To explore the molecular mechanism(s) underlying the link evidenced between MGO stress and AKT activation, we next envisaged the possibility that Hsp27 could be implicated, knowing that (1) MGO -glycated Hsp27 (MGO-Hsp27) in cancer cells supports their escape from apoptosis (Oya-Ito et al., 2011; Sakamoto et al., 2002), (2) Hsp27 chaperone activity has been associated with the resistance to different cytotoxic agents (Kamada et al., 2007; Kuramitsu et al., 2012; Mori-Iwamoto et al., 2007), and (3) Hsp27 has been shown to control apoptosis by regulating AKT activation (Rane et al., 2003). First, we undertook the detection of MGO-Hsp27 in SW48 isogenic model. Immunoprecipitation (IP) of argpyrimidine MGO adducts in KRAS^{WT} and KRAS^{G12V} cells evidenced Hsp27 detection using western blotting and confirmed the presence of MGO-Hsp27 in these cells, with significantly elevated amounts in KRAS^{G12V} when compared with KRAS^{WT} cells (Figure 5E). Consistently, the reverse IP experiment using anti-Hsp27 antibody allowed the detection of an argpyrimidine adduct of the expected molecular weight (~27 kDa) (Figure 5F). Interestingly, the screening of a series of human CRC cell lines showed that elevated amounts of MGO-Hsp27 paralleled high P-AKT levels (Figure 5G). At this point, our observations let us envisage that activation of AKT in CRC cells is associated with MGO stress and high MGO-Hsp27 levels. Previous studies demonstrated that MGO-Hsp27 is more prone to form stable and functional oligomers than its native form (Oya-Ito et al., 2011; Sakamoto et al., 2002). Our *in vitro* glycation of recombinant human Hsp27 (rhHsp27) by MGO (500 μM) notably favored the formation of MGO-Hsp27 dimers that were present endogenously and detectable in KRAS^{G12V}, but not in KRAS^{WT}, protein extracts (Figure S4A). Knowing that Hsp27 plays a role in AKT activation, we aimed at exploring further the marked difference between KRAS^{G12V} and KRAS^{WT} cells in term of MGO-Hsp27 level. We used cycloheximide to block protein synthesis and measure the half-life of Hsp27 in the SW48 model. In KRAS^{WT} cells, total Hsp27 (with predominantly native Hsp27) decreased rapidly with time (half-life was reached after 7.3 h) when compared with total Hsp27 level (with predominantly MGO-Hsp27) of KRAS^{G12V} cells, which showed elevated and stable levels, as shown in Figure S4B and quantified in Figure S4C. The specific detection of MGO-Hsp27 level further completed this observation, as MGO-Hsp27 was detected in both cell lines all along cycloheximide challenge (Figure S4B). In KRAS^{WT} cells, the decrease of total Hsp27 in favor of cellular enrichment in stable MGO-Hsp27 was associated with the specific increase of P-AKT levels (Figure S4B). The relationship revealed between MGO-Hsp27 and AKT activation was further assessed in experiments where BioPORTER reagent was used to deliver rhHsp27 or its *in vitro* glycated form, MGO-rhHsp27, into cells by endocytosis. We observed a significant increase of P-AKT upon MGO-rhHsp27 delivery to

(E) GLO1 protein levels assessed in CRC cells using western blot. β-Actin was used for normalization. A representative western blot of at least three independent experiments is shown.

(F) GLO1 maximal activity measured in CRC cells is expressed as A.U. per mg proteins. Data were analyzed using unpaired Student's t test and shown as mean values ± SEM of three independent experiments.

**$p < 0.01$; *$p < 0.05$; ns, not significant. See also Figure S2.

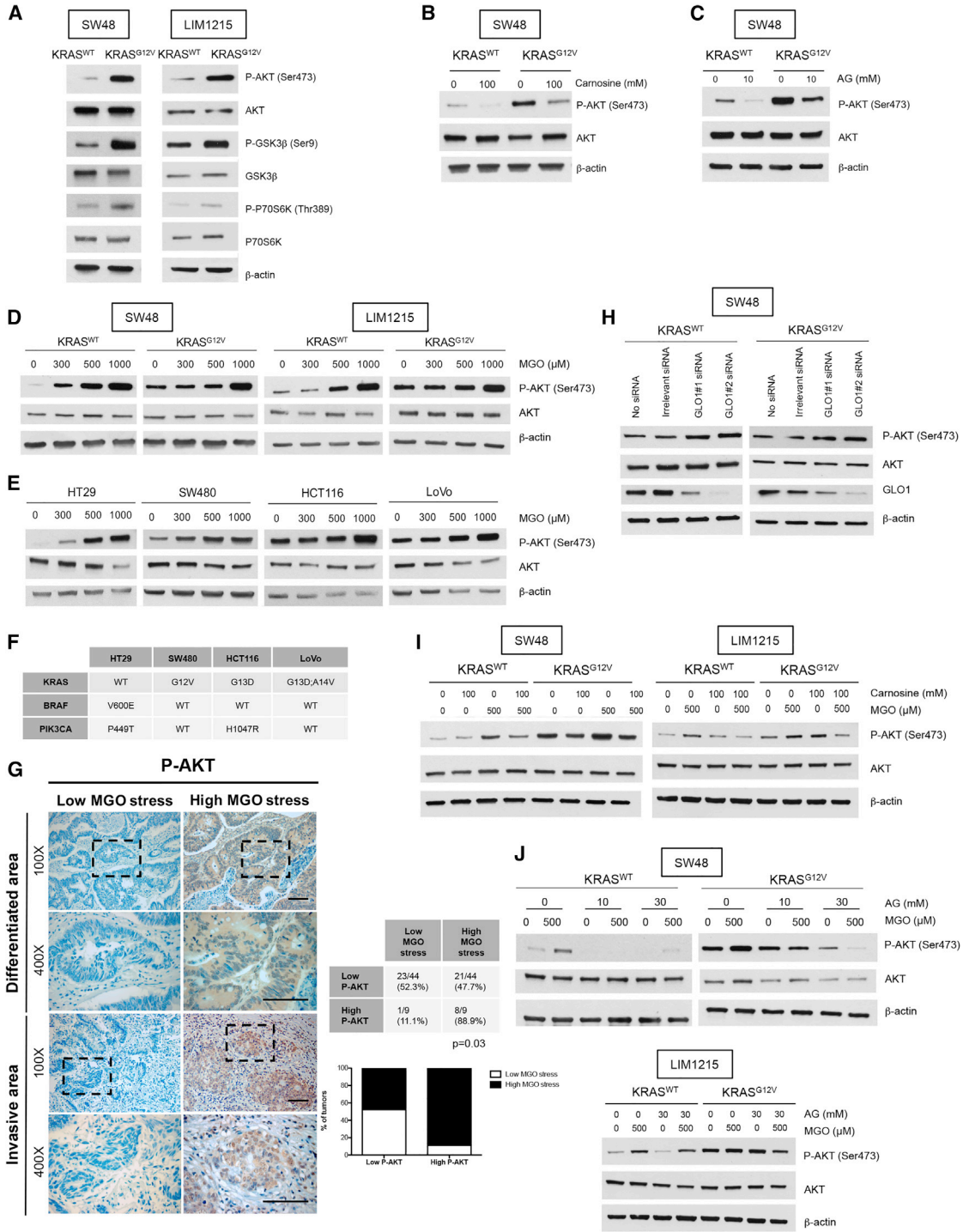

Figure 4. MGO Stress Induces AKT Activation in CRC Cells that Is Reverted Using MGO Scavengers

(A) Basal levels of P-AKT, P-GSK3β, and P-P70S6K in CRC cells.

(B and C) Basal P-AKT level is decreased upon carnosine (100 mM, 24 h) (B) and aminoguanidine (10 mM, 24 h) (C) treatment in CRC cells.

(D) P-AKT level was assessed after 3 h of MGO treatment at the indicated doses in CRC isogenic models.

(E) P-AKT level was assessed after 3 h of MGO treatment at the indicated doses in the indicated human CRC cell lines.

(F) Oncogenic mutations of the CRC cell lines shown in E.

(G) P-AKT IHC staining in low- and high-MGO stress colon tumors as assessed by their argpyrimidine level. Two representative low and high MGO stress CRC tumors are shown. Data were analyzed using Fisher's test ($p = 0.03$). The lower images show the area within the dashed rectangle on the upper images at higher magnification. Scale bars represent 100 μm.

(legend continued on next page)

SW48 KRAS^{WT} cells (Figure 5H). Next, we used specific siRNAs directed against Hsp27 in KRAS^{WT} and KRAS^{G12V} cells treated with MGO. In the absence of MGO-Hsp27, exogenous MGO treatment was less efficient at inducing P-AKT (Figure 5I). The ultimate demonstration of the role of endogenous MGO-Hsp27 in AKT activation arose from carnosine (Figure 5J) and aminoguanidine (Figure 5K) treatments, which induced a significant decrease of MGO-Hsp27 in KRAS^{G12V} cells that was paralleled by P-AKT inhibition in CRC cells.

Carnosine Specifically Inhibits KRAS^{G12V} Cell Clonogenic Potential *In Vitro* and Tumor Growth *In Vivo*

After having established the potent effect of carnosine as an inhibitor of AKT activity in CRC cells. We next aimed at demonstrating the crucial dependence of KRAS-mutated CRC cells on AKT for their survival. In fact, significantly lower concentrations of LY294002 and BYL719 (PI3K inhibitors) and MK2206 (AKT inhibitor) were necessary to decrease by half the viability of KRAS-mutated cells when compared with wild-type cells (Figure 6A). KRAS^{G12V} showed a significant apoptotic death when challenged with PI3K/AKT inhibition, while KRAS^{WT} cells did not (Figure 6B), thus validating the higher dependency of KRAS-mutated cells on AKT activation. Efficient inhibition of AKT phosphorylation in presence of each inhibitor is shown in Figure S5A.

We next compared the capacity for continued proliferation of KRAS^{WT} and KRAS^{G12V} cells in presence of carnosine. Clonogenic assay performed on SW48 model showed a lower capacity of KRAS^{G12V} cells to produce colonies in presence of carnosine when compared with KRAS^{WT} (Figure 6C). Accordingly, KRAS^{G12V} cells proved to be significantly more sensitive to carnosine treatment in comparison with KRAS^{WT} cells (Figure 6D). Carnosine provoked a 2.3-fold increase of apoptosis in SW48 KRAS^{G12V} as assessed using Annexin V assay (Figure 6E), while KRAS^{WT} did not show any significant apoptosis change at the same dose. Likewise, aminoguanidine treatment induced apoptosis only in KRAS-mutated cells (Figure 6E). In presence of both MGO scavengers (Figure 6F), KRAS^{G12V} cells showed a strong increase of cleaved poly (ADP-ribose) polymerase (PARP) and cleaved caspase 3 apoptosis markers. Evidence sustaining carnosine pro-apoptotic effect via AKT inhibition was brought using SC-79, a specific AKT activator. The effect of SC-79 on carnosine-induced apoptosis was evaluated by pretreating KRAS^{G12V} cells with increasing doses of SC-79 beginning 2 h before the addition of carnosine. The percentage of apoptotic cells was globally decreased in the presence of SC-79 and reached significance at the higher dose used (Figure 6G), thus demonstrating that carnosine cytotoxicity occurred, at least in part, via AKT inhibition in KRAS-mutated cells. The efficacy of SC-79 at inducing P-AKT was verified by western blotting (Figure S5B).

We next tested carnosine's effect on the growth of subcutaneous SW48 KRAS^{G12V} and KRAS^{WT} xenografts in mice. Remarkably, intraperitoneal injections of carnosine induced a significant decrease in KRAS^{G12V} tumor growth but had no impact on KRAS^{WT} cells (Figure 6H). MGO adducts, Hsp27, P-AKT, and Ki67 IHC detection performed on experimental tumors showed a consistent decrease in KRAS^{G12V} tumors treated with carnosine and brought their levels to those of KRAS^{WT} cells (Figures 6I). These *in vivo* data are in good complementarity with *in vitro* observations, as they point to the particular reliance of KRAS^{G12V} cells on MGO stress and demonstrate the anti-tumor efficacy of carnosine against KRAS-mutated CRC tumors.

Carnosine Resensitizes KRAS-Mutated CRC Cells to Cetuximab *In Vitro* and *In Vivo*

Our demonstration of the importance of MGO stress for KRAS^{G12V} survival and tumor growth prompted us to test the possibility that carnosine could resensitize KRAS-mutated CRC cells when used in combination with cetuximab. As expected, cetuximab treatment of SW48 KRAS^{G12V} cells did not induce a significant increase of their apoptotic rate (Figure 7A). In comparison, carnosine tripled the proportion of apoptotic cells. Moreover, co-treatment with cetuximab and carnosine proved to be more efficient than each treatment considered alone (Figure 7A). Thus, the shutdown of the AKT major survival pathway using carnosine resensitized KRAS-mutated cells to cetuximab. Enhanced apoptosis upon combined treatment was further underlined by increased PARP cleavage and caspase 3 (Figure 7B). To strengthen these important conclusions, we next conducted *in vivo* experiments where we treated mice bearing KRAS-mutated SW48 (Figure 7C), HCT116 (Figure 7D), and LIM1215 (Figure 7E) tumors with both cetuximab and carnosine. Combined treatment showed a significant blockade of tumor growth compared with separate cetuximab and carnosine treatments. Altogether, these data support the rationale for combining cetuximab with MGO scavenger molecules in the mutant KRAS CRC genetic setting.

Induction of MGO Stress Renders Sensitive LIM1215 Cells Resistant to Cetuximab

Based on these results, we reasoned that the induction of MGO stress in KRAS^{WT} LIM1215 cells that are sensitive to cetuximab should induce P-AKT and ultimately decrease their sensitivity to cetuximab. To test this hypothesis, we generated KRAS^{WT} LIM1215 cells stably depleted for GLO1 using specific small hairpin RNAs (shRNAs). In these cells, the induction of endogenous MGO stress was evidenced by the detection of MGO adducts (Figure 7F) and intracellular MGO level quantification using MBo probe (Figure 7G). MGO-stressed cells showed a significant induction of P-AKT (Figure 7H) and proved to be resistant to cetuximab, as demonstrated by their respective growth curves (Figure 7I) and cetuximab half-maximal inhibitory concentration (IC_{50}) calculation (Figure 7J). Collectively, these data indicate that MGO stress induces AKT activation and confers resistance to cetuximab in wild-type KRAS CRC cells. In fact, the MGO

(H) P-AKT induction was assessed upon GLO1 silencing using two siRNAs in CRC cells. Efficient GLO1 silencing is shown.
(I and J) The induction of P-AKT by MGO is reverted by carnosine (I) and aminoguanidine (J) after 3 h of co-treatment in CRC cells. All immunoblots were normalized for β-actin and are representative of at least three independent experiments.
See also Figure S3.

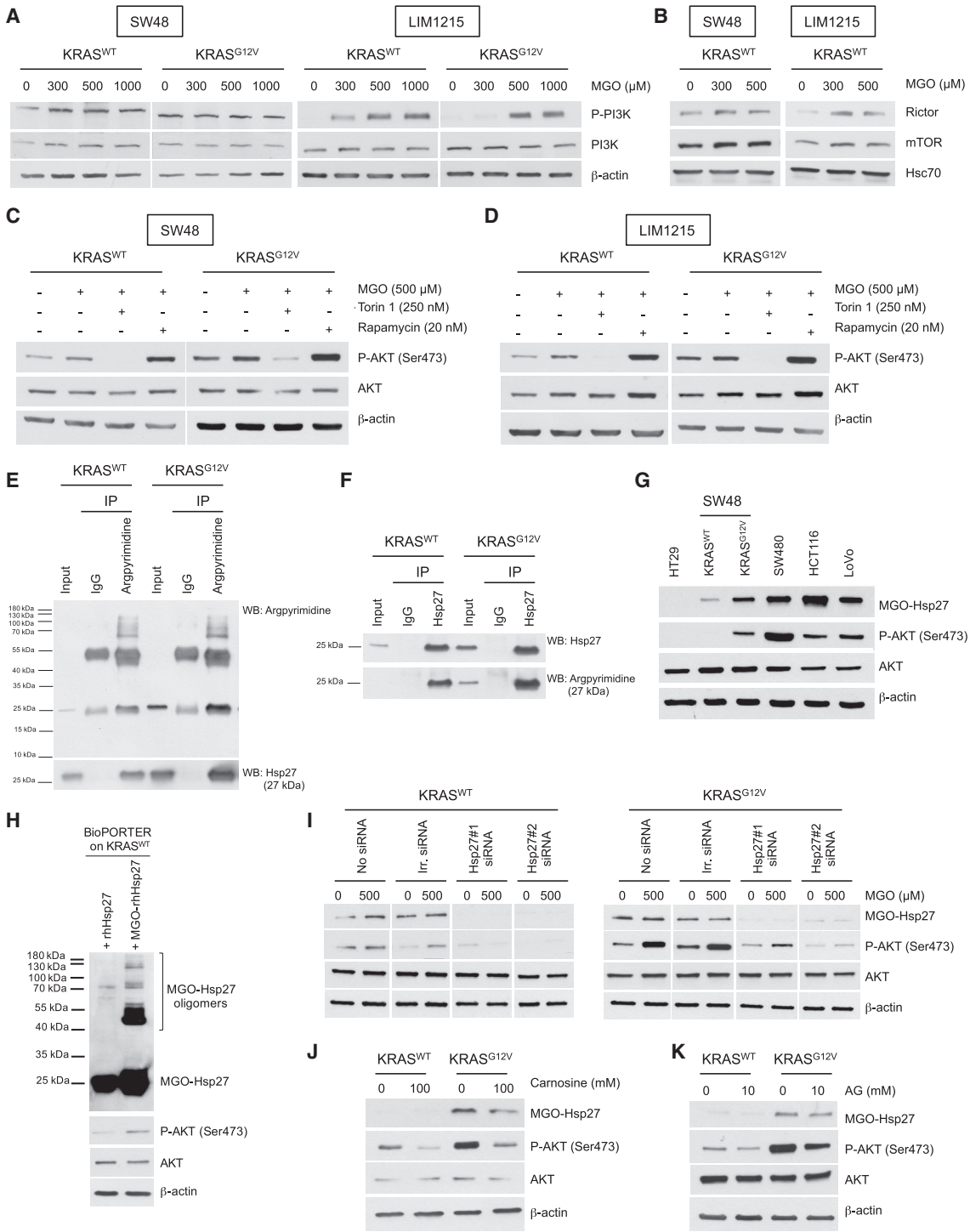

Figure 5. The PI3K/mTORC2 Axis and MGO-Hsp27 Accumulation Contribute to MGO-Mediated AKT Activation in CRC Cells

(A) Western blot detection of P-PI3K and PI3K in CRC cells upon MGO treatment (3 h) at the indicated concentrations. β-Actin was used for normalization.

(B) Western blot detection of Rictor and mTOR in KRAS^{WT} CRC cells upon MGO treatment (3 h) at the indicated concentrations. Hsc70 was used for normalization.

(C and D) Levels of P-AKT and AKT were assessed after 3-h co-treatment with MGO and torin 1 or rapamycin in SW48 (C) and LIM1215 (D) CRC cells. β-Actin was used for normalization.

(E) IP of MGO-adducts in SW48 CRC cells using anti-argpyrimidine monoclonal antibody. Mouse immunoglobulin G (IgG) was used as control. Total cell lysates (input) and IPs were immunoblotted (WB) using the indicated antibodies.

(legend continued on next page)

stress condition recapitulates by itself the features of mutant KRAS resistance to cetuximab and therefore could explain, at least in part, the lack of efficacy of this drug in the majority of advanced CRC patients with wild-type KRAS tumors.

DISCUSSION

Energetic metabolism adaptation is a characteristic feature of cancer (Hanahan and Weinberg, 2011). Metabolic pathways such as glycolysis are notably rewired in order to divert glucose into anabolic pathways to satisfy the demand for cellular building blocks (Vander Heiden et al., 2009). These last decades, the study of oncometabolites such as MGO has attracted much interest, as they point to cancer cell properties that could be therapeutically exploited in different types of cancer (Sullivan et al., 2016). Changes in the levels of specific metabolites have been implicated in cancer initiation, progression, and drug resistance.

The reprogramming of tumor metabolism is notably under the control of oncogenic signals. In particular, the RAS oncogene has been shown to promote glycolysis (Racker et al., 1985; Yun et al., 2009). MGO levels in cancer cells result from the balance between MGO formation, mainly as a by-product of glycolysis, and its detoxification by the glyoxalase system (Bellahcène et al., 2018). In this study, we demonstrate that mutant KRAS tumors showed elevated MGO adducts when compared with wild-type KRAS CRC tumors. $KRAS^{G12V}$ and $KRAS^{WT}$ isogenic CRC cell lines presented with similar GLO1 detoxification activity, thus indicating that it is MGO production and adducts formation that are favored in mutant-KRAS cells. Consistently, glucose tracing experiments proved that the glycolytic flux is intensified in mutant KRAS when compared with wild-type cells and that glucose is the main source of MGO in CRC cells. The concept defining cancer cell dependence on glycolysis to resist to targeted therapy has been well documented in melanoma. Indeed, BRAF inhibitors possess anti-glycolytic activity, and glucose metabolism is restored upon development of acquired resistance in melanoma (Hardeman et al., 2017; Parmenter et al., 2014). Consistently, cetuximab proved to reverse the Warburg effect in head and neck squamous cell carcinoma (HNSCC) through HIF-1 alpha inhibition, and HNSCC cells with acquired cetuximab resistance expressed high HIF-1 alpha levels and were highly glycolytic (Lu et al., 2013).

We demonstrated that an important consequence of the MGO stress condition in CRC cells is the activation of AKT signaling. MGO consistently increased the phosphorylation of AKT, even over a high basal level, in all CRC cell lines analyzed independently of their mutational profile. AKT activation was reversed using MGO scavengers, thus establishing a direct link between MGO oncometabolite and this key pro-survival signaling pathway in CRC. We have shown that $KRAS^{G12V}$ cells rely on the PI3K/AKT pathway for their survival and that experimental tumors show significantly decreased growth inhibition in the presence of carnosine. On the contrary, $KRAS^{WT}$ tumors and cells presented with low MGO stress and P-AKT and were less dependent on AKT activity for their survival. Accordingly, they proved to be insensitive to MGO stress blockade when xenografted in mice.

Approximately one-fourth of human CRC tumors harbor mutations in both KRAS and PI3KCA (Parsons et al., 2005). The selective advantage conferred by such apparently redundant signalization has been notably associated with an aggravated resistance to anti-EGFR therapy (Jhawer et al., 2008) and the suppression of oncogene-induced senescence (Kennedy et al., 2011). In the context of MGO stress, another non-negligible benefit from AKT activation is its well-known role as a driver of the Warburg effect. For example, AKT triggers increased glucose uptake through the upregulation of glucose transporters (Elstrom et al., 2004; Courtnay et al., 2015), resulting in enhanced glycolytic flux, cell growth, and survival (Robey and Hay, 2009). These observations let us propose a vicious cycle where MGO stress triggers AKT activity that in turn sustains the glycolytic flux, which then produces more MGO in cancer cells.

Cetuximab therapy is aimed at targeting the major pathways activated through EGFR. Based on their screening of 22 CRC cell lines for cetuximab response, Jhawer and collaborators (Jhawer et al., 2008) concluded that the cell lines that acquire constitutive activation of the PI3K/AKT pathway have a diminished dependence on canonical EGFR-ligand-induced signaling and are more resistant to cetuximab. One important finding of our study is that sensitive $KRAS^{WT}$ cells that undergo MGO stress switch to a dominant AKT dependence for their survival and become resistant to cetuximab. Altogether, these results not only point to pro-survival signals induced by MGO stress contributing, at least in part, to cetuximab resistance in mutant KRAS condition but also provide essential information for understanding the resistance to EGFR-targeted therapy reported in wild-type KRAS clinical setting. In fact, up to 50% of patients with wild-type KRAS tumors are resistant to cetuximab, and the quest for predictive biomarkers and new therapeutic targets is still the object of intense research (De Roock et al., 2011; Salgado et al., 2018). We propose MGO-mediated AKT activation as an additional mechanism of resistance to cetuximab that does not involve the well-described genetic alterations affecting downstream and cross-talk effectors of EGFR signaling shown to negatively affect sensitivity to EGFR inhibitors (De Roock et al., 2010; Di Nicolantonio et al., 2008; Sartore-Bianchi et al., 2009). It would be interesting to check whether MGO stress status could predict, among quadruple wild-type CRC tumors

(F) Reverse IP using anti-Hsp27 allowed the detection of an ~27-kDa argpyrimidine adduct corresponding to MGO-Hsp27.
(G) Parallel detection of MGO- Hsp27 and P-AKT in the indicated human CRC cells.
(H) Recombinant human Hsp27 (rhHsp27) or MGO-Hsp27 (MGO-rhHsp27) was introduced into SW48 $KRAS^{WT}$ cells with BioPORTER as described in STAR Methods. The effect of MGO-rhHsp27 on AKT activation is shown.
(I) Loss of MGO-mediated AKT activation in MGO-Hsp27-depleted cells using specific siRNAs directed against Hsp27.
(J and K) Detection of MGO-Hsp27 and P-AKT levels in SW48 $KRAS^{WT}$ and $KRAS^{G12V}$ cells upon carnosine (100 mM, 3 h) (J) and aminoguanidine (10 mM, 6 h) (K) treatment. β-Actin was used for normalization. All western blots are representative of at least three independent experiments.
See also Figure S4.

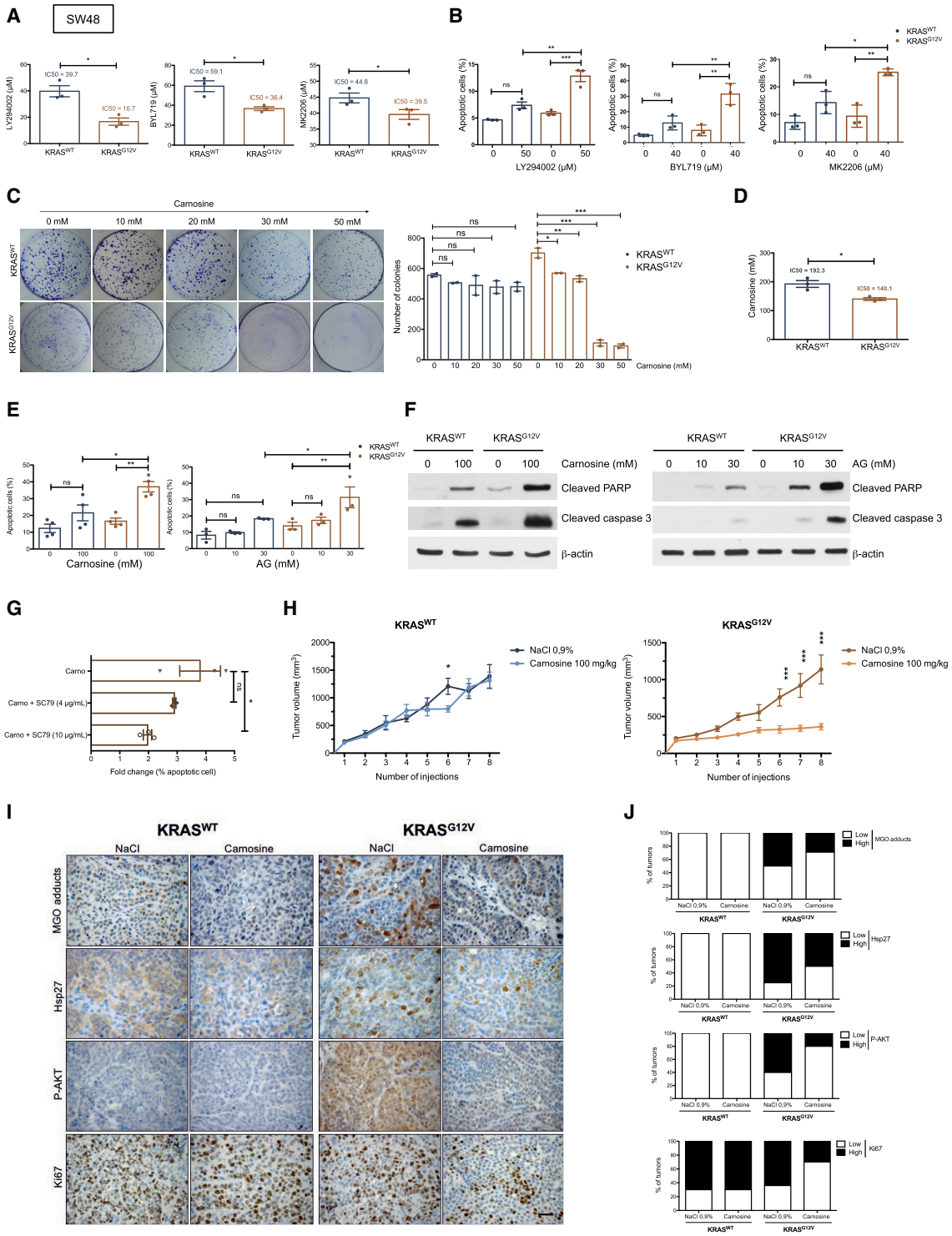

Figure 6. Carnosine Specifically Inhibits KRAS^{G12V} Cell Survival through AKT Inhibition

(A) Determination of half-maximal inhibitory concentration (IC_{50}) for LY294002, BYL719, and MK2206 in SW48 CRC cells as described in STAR Methods. Data were analyzed using an unpaired Student's t test and shown as mean values ± SEM of three independent experiments.

(B) Apoptosis analysis in CRC cells treated with LY294002 (50 μM, 8 h), BYL719 (40 μM, 24 h), and MK2206 (40 μM, 24 h). Annexin-V-positive cells were quantified and shown as the percentage of apoptotic cells. All data are presented as mean values ± SEM of three independent experiments and were analyzed using two-way ANOVA followed by Bonferroni's test.

(legend continued on next page)

(KRAS/NRAS/BRAF/PI3KCA), those that display MGO-induced dependence on PI3K/AKT for their survival and will be refractory to cetuximab treatment but sensitive to MGO blockade.

The accumulated evidence indicates that the mechanisms that cause primary resistance can also be responsible of acquired resistance to cetuximab (i.e., HER2 and MET amplifications and genetic alterations of RAS/RAF/MEK) (Bray et al., 2019; Li et al., 2019; Troiani et al., 2016; Van Emburgh et al., 2014). We cannot exclude that MGO-mediated AKT activation occurring upon glycolytic switch (triggered by KRAS mutation or other mechanisms) could also play a role in acquired resistance to EGFR-targeted therapies in CRC. Reliable preclinical models recently validated such as xenospheroids generated from patient-derived xenografts (Luraghi et al., 2018) will prove very useful to broaden our understanding of the role of glycolysis-induced MGO stress in acquired resistance to anti-EGFR therapy in CRC.

Being a critical regulator of AKT activity, mTORC2 protein kinase lately gained more attention as a key player in cancer cell survival, energetic metabolism, and proliferation. We show that MGO-stress-mediated AKT activation depends, at least in part, on the induction of mTORC2 expression in CRC cells. These findings provide with an unanticipated mechanism of regulation of mTORC2, which receives inputs mainly from growth factors and cytokines. Mechanistically, we also demonstrated that endogenous and exogenous MGO stress induces AKT activation that is lost upon Hsp27 silencing. AKT is a known target for Hsp27 chaperone activity, which prevents its dephosphorylation and degradation, hence promoting its stability and activation (Mearow et al., 2002). Hsp27 expression is increased in a variety of malignancies, including gastric (Huang et al., 2010) and pancreatic (Melle et al., 2007) cancers, and its overexpression is a bad prognostic factor in CRC (Han et al., 2018; Yu et al., 2010). MGO modification of Hsp27 has been previously shown to be essential to its repressing activity on caspase activation and cancer cell evasion from apoptosis (Oya-Ito et al., 2011; Sakamoto et al., 2002; van Heijst et al., 2006). Our demonstration of high levels of stable MGO-Hsp27 in mutant KRAS CRC cells appears to be of crucial importance in the context of their resistance to anti-EGFR therapy. Taken collectively, these studies and ours let us propose that the detection of global MGO adducts levels or specific MGO stress adducts such as MGO-Hsp27 could represent an interesting prediction tool to help stratify patients likely to benefit from anti-EGFR therapy.

Given the difficulties associated with directly inhibiting the KRAS oncoprotein, treating mutant KRAS CRC remains a major challenge. EGFR signaling represents the main convergent pathway that is intensively explored in preclinical studies and clinical trials for a better understanding of anti-EGFR therapy resistance in CRC. The complexity of the EGFR/MEK/ERK signaling network involves numerous feedback loops and extensive cross-talk nodes with other signaling pathways and compensatory pathways, providing ample opportunities for circumventing the effects of MEK and PI3K/mTOR inhibitors used alone or in combination with EGFR blockade. A recent excellent review recapitulates the mechanisms of primary and secondary resistance to anti-EGFR therapy and presents the numerous related clinical trials and their conclusions (Parseghian et al., 2019). In fact, most of the resistance mechanisms revealed aberrant reactivation of key intracellular signals that were basically targeted by the drugs. For example, inhibition of AKT unexpectedly reactivated receptor tyrosine kinase signaling and expression, thereby inducing PI3K, ERK, and other crucial effectors (Chandarlapaty et al., 2011). Several studies highlighted the importance of PI3K/AKT pathway activation as an escape mechanism underlying acquired resistance in response to an MEK inhibitor (Turke et al., 2012) or combined cetuximab/MEK therapy (Vitiello et al., 2019) in KRAS-mutated CRC cell lines.

One key finding of this study is the resensitization to cetuximab of KRAS-mutated cells using MGO scavengers. Carnosine has been previously shown to exert anti-proliferative effects against cancer cells (Iovine et al., 2012; Lee et al., 2018), and oncolytic adenoviruses loaded with carnosine showed anti-tumor activity in *vitro* and *in vivo* (Garofalo et al., 2016). Until recently, the potential therapeutic use of carnosine in human has been limited by serum and tissue carnosinases. Carnosinol, a stable carnosine analog with high oral bioavailability and resistant to

(C) Representative pictures of the clonogenic assay performed in presence of increased concentrations of carnosine. Colonies were counted as described in STAR Methods, and numbers of colonies are presented as mean ± SEM of two independent experiments.

(D) Determination of IC_{50} for carnosine in SW48 CRC cells as described in STAR Methods. Data were analyzed using unpaired Student's t test and are shown as mean values ± SEM of three independent experiments.

(E) Apoptosis analysis in SW48 CRC cells treated with carnosine (100 mM, 48 h) and aminoguanidine (10 and 30 mM, 48 h). Annexin-V-positive cells were quantified and shown as the percentage of apoptotic cells. All data are presented as mean values ± SEM of three independent experiments and were analyzed using one-way ANOVA followed by Bonferroni's test.

(F) Cleaved PARP and cleaved caspase-3 apoptosis markers in SW48 CRC cells in parallel experiment as in E.

(G) Apoptosis analysis in SW48 $KRAS^{G12V}$ CRC cells treated with carnosine (200 mM, 24 h) and pretreated with SC79 at the indicated concentrations for 2 h. Annexin-V-positive cells were quantified and shown as the percentage of apoptotic cells. Each fold change of percentage of apoptotic cells was quantified relative to its corresponding control condition. All data are presented as mean values ± SEM of three independent experiments and were analyzed using one-way ANOVA followed by Bonferroni's test.

(H) SW48 $KRAS^{WT}$ and $KRAS^{G12V}$ CRC cells were injected subcutaneously in the flank of NOD-SCID mice (20 mice/group). Mice were treated with carnosine by intraperitoneal injection (100 mg/kg, 3 times/week). After 8 carnosine injections, mice were sacrificed and primary tumors were collected. Data are shown as mean values ± SEM.

(I) Experimental tumors were subjected to IHC staining of MGO adducts, Hsp27, P-AKT, and Ki67 proliferation marker. Representative pictures of carnosine- or vehicle-(NaCl)-treated experimental tumors are shown. Scale bar represents 100 μm.

(J) The proportion of experimental tumors presenting the indicated immunostaining scores (low and high) for MGO adducts, Hsp27, P-AKT, and proliferation rate Ki67, as defined in STAR Methods, is shown. Data were analyzed using one-way or two-way ANOVA depending on the number of grouping factors. Dunnett's or Bonferroni's tests were applied for simple or multiple comparisons, respectively. ***$p < 0.001$, **$p < 0.01$, and *$p < 0.05$; ns, not significant.

See also Figure S5.

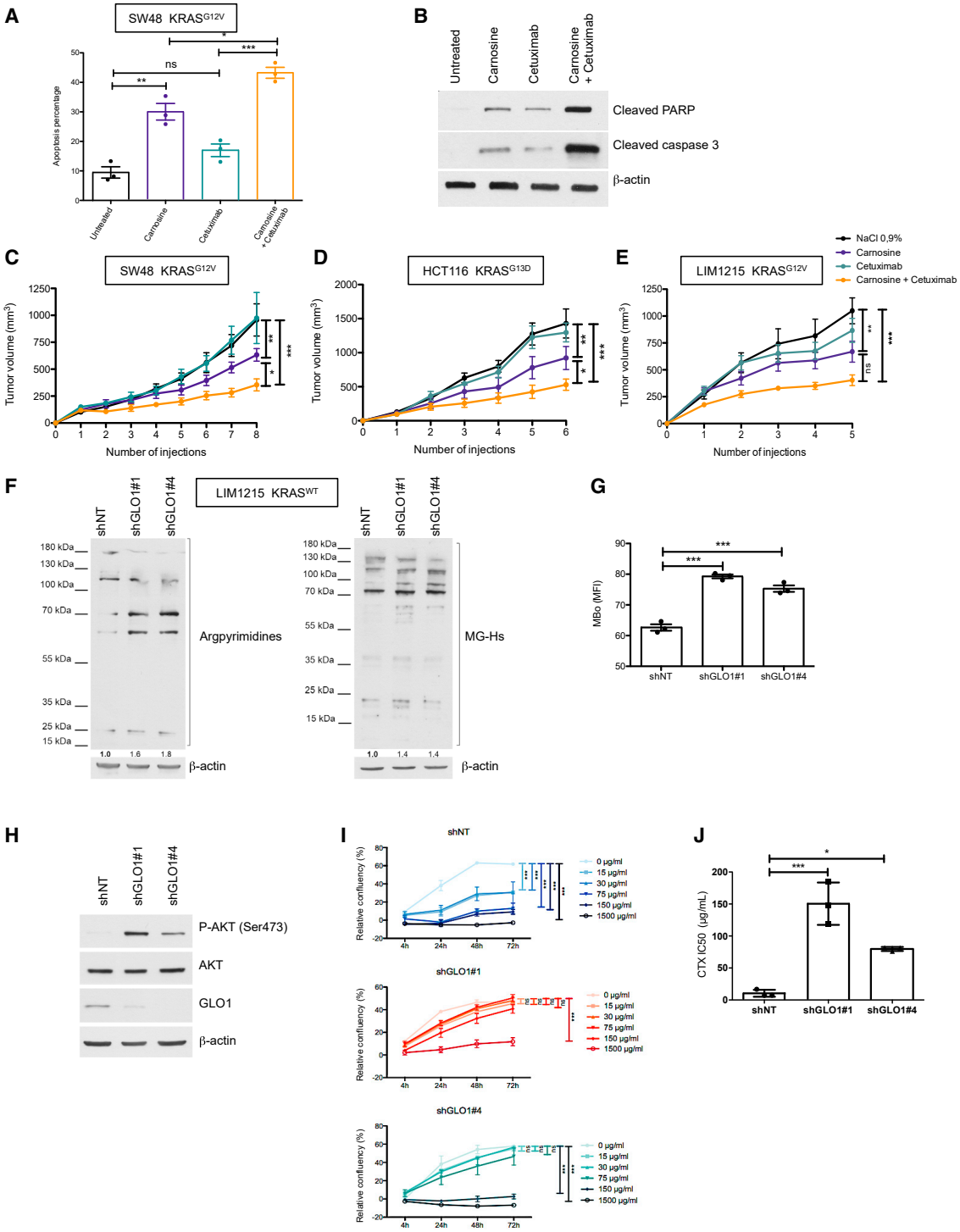

Figure 7. Carnosine Resensitizes KRAS-Mutated CRC Cells to Cetuximab, and the Induction of MGO Stress Is Sufficient to Render LIM1215-Sensitive Cells Resistant to Cetuximab

(A) Apoptosis analysis of CRC cells treated with cetuximab (30 μg/mL, 48 h) in the presence of carnosine (100 mM, 48 h). Annexin-V-positive cells were quantified, and data are presented as mean values ± SEM of three independent experiments. One-way ANOVA was performed followed by Bonferroni's test.

(B) Cleaved PARP and cleaved caspase-3 were assessed in KRAS^{G12V} cells in the same conditions as in A.

(C–E) SW48 KRAS^{G12V} (C), HCT116 KRAS^{G13D} (D), and LIM1215 KRAS^{G12V} (E) CRC cells were injected subcutaneously in the flank of NOD-SCID mice (6–10 mice/group). Mice were treated with carnosine (100 mg/kg, 3 times/week) and/or cetuximab (0.5 mg/treatment, 2 times/week). Mice were sacrificed, and tumors were collected. All data are shown as mean values ± SEM and were analyzed using two-way ANOVA.

(legend continued on next page)

carnosinases, has been recently developed and proposed to treat obesity-related metabolic disorders (Anderson et al., 2018). Considerable attention has been given to the use of natural substances as anticancer drugs. This is even more crucial when proposing combination therapeutic strategies to achieve efficacy against resistant tumors and to observe meaningful clinical benefit. Indeed, the emergence of doublet or triplet combinations tested clinically to overcome acquired resistance to cetuximab will expectedly have additional toxicities for the patients. We propose that stable carnosine analogs, such as carnosinol, administered in combination with cetuximab could be not only an effective but also a safe anti-tumor therapy. Future studies are needed to strengthen the rationale for combining anti-EGFR therapy with MGO scavengers to treat resistant glycolytic tumors harboring or not oncogenic RAS mutations.

In sum, our data underscore the importance of taking into account energetic metabolic dysregulation next to tumor genotyping when stratifying CRC patients prior to EGFR-targeted therapy.

STAR★METHODS

Detailed methods are provided in the online version of this paper and include the following:

- KEY RESOURCES TABLE
- LEAD CONTACT AND MATERIALS AVAILABILITY
- EXPERIMENTAL MODEL AND SUBJECT DETAILS
  - Clinical tumor samples
  - Cell lines
  - Mouse xenografts
- METHOD DETAILS
  - Mutational status analysis using NGS
  - Immunohistochemistry (IHC)
  - Seahorse analysis
  - Metabolomics
  - MGO measurement
  - Cellular MGO quantification
  - Western blot analysis
  - D-lactate dosage
  - GLO1 activity
  - Determination of half-maximal inhibitory concentrations 50 (IC_{50})
  - Apoptosis assay
  - Immunoprecipitation
  - BioPORTER assay
  - siRNA and shRNA transfections
  - Protein stability
  - Clonogenic assay
  - Real-time proliferation assay
- QUANTIFICATION AND STATISTICAL ANALYSIS
  - Evaluation of immunohistochemical staining
- DATA AND CODE AVAILABILITY

SUPPLEMENTAL INFORMATION

Supplemental Information can be found online at https://doi.org/10.1016/j.celrep.2020.01.012.

ACKNOWLEDGMENTS

J.B. is a Télévie PhD research fellow and A. Bellahcène. is a research director at the National Fund for Scientific Research (FNRS), Belgium. The authors are thankful to S. Nüchtern and V. Hennequière for expert technical assistance. We thank Dr. K. Uchida (University of Tokyo, Japan) and Dr. D. Spiegel (Yale University, USA) for kindly providing anti-argpyrimidine antibody and MBo probe, respectively. The authors are thankful to Dr. S. Gofflot (CHU/ULiège Biobank) and Pr. A-F. Donneau (Department of Public Health, University of Liège). The authors acknowledge the scientific and technical support provided at the animal, imaging and flow cytometry, genomics, viral vectors, and immunohistology technology platforms of the GIGA-Research Institute (University of Liège, Belgium). This work was supported by a grant from Télévie-FNRS (J.0007.19) awarded to A. Bellahcène. We thank the FNRS, University of Liège, and Fondation Léon Fredericq for support. A. Blomme, G.M. MacKay, and H.Y. Leung were supported by Cancer Research UK Beatson Institute core funding (C596/A17196) and CRUK core group awarded to H.Y.L (A22904).

AUTHOR CONTRIBUTIONS

J.B., V.C., and A. Bellahcène conceived and designed the experiments. J.B., M.-J.N., M.C., A.T., A. Blomme, J.L.S., B.K., G.M.M., B. Chiavarina, B. Costanza, G.R., F.D., F.A., and N.M. performed the experiments and acquired data. J.B., M.-J.N., M.C., A.T., A. Blomme, J.L.S., B.K., G.M.M., B. Chiavarina, B. Costanza, G.R., H.Y.L., F.D., F.L., V.B., C.G.S., O.P., V.C., and A. Bellahcène analyzed the data. P.L. and R.H. provided and evaluated clinical information. P.G.C. provided with essential reagents. J.B. and A. Bellahcène wrote the main manuscript text. All authors critically reviewed and approved the final manuscript.

DECLARATION OF INTERESTS

The authors declare no competing interests.

Received: April 2, 2019
Revised: November 10, 2019
Accepted: January 2, 2020
Published: February 4, 2020

REFERENCES

Alamo, P., Gallardo, A., Di Nicolantonio, F., Pavón, M.A., Casanova, I., Trias, M., Mangues, M.A., Lopez-Pousa, A., Villaverde, A., Vázquez, E., et al. (2015). Higher metastatic efficiency of KRas G12V than KRas G13D in a colorectal cancer model. FASEB J. *29*, 464–476.

(F) Western blot detection of MGO adducts (argpyrimidines and MG-Hs) in LIM1215 CRC cells stably depleted for GLO1 using shRNAs.
(G) Intracellular MGO in LIM1215 upon GLO1 silencing using shRNAs was assessed by flow cytometry using an MBo-specific fluorescent probe. Data are shown as mean values ± SEM of three independent experiments. Data were analyzed using one-way ANOVA followed by Dunnett's test.
(H) P-AKT induction was assessed upon GLO1 silencing using shRNAs in LIM1215 CRC cells. Efficient GLO1 silencing is shown.
(I) Proliferation assay as assessed using IncuCyte in LIM1215 shNT, shGLO1#1, and shGLO1#4 CRC cells upon cetuximab treatment at the indicated time and concentrations. Data are shown as mean values ± SEM of one representative experiment out of three. Data were analyzed using two-way ANOVA followed by Bonferroni's test.
(J) Determination of IC_{50} for cetuximab in LIM1215 shNT, shGLO1#1, and shGLO1#4 CRC cells as described in STAR Methods. Data were analyzed using unpaired Student's t test and shown as mean values ± SEM of three independent experiments. ***$p < 0.001$, **$p < 0.01$, *$p < 0.05$; ns, not significant.

Allegra, C.J., Rumble, R.B., Hamilton, S.R., Mangu, P.B., Roach, N., Hantel, A., and Schilsky, R.L. (2016). Extended ras gene mutation testing in metastatic colorectal carcinoma to predict response to anti-epidermal growth factor receptor monoclonal antibody therapy: American Society of Clinical Oncology Provisional Clinical Opinion Update 2015. J. Clin. Oncol. *34*, 179–185.

Anderson, E.J., Vistoli, G., Katunga, L.A., Funai, K., Regazzoni, L., Monroe, T.B., Gilardoni, E., Cannizzaro, L., Colzani, M., De Maddis, D., et al. (2018). A carnosine analog mitigates metabolic disorders of obesity by reducing carbonyl stress. J. Clin. Invest. *128*, 5280–5293.

Bardelli, A., and Siena, S. (2010). Molecular mechanisms of resistance to cetuximab and panitumumab in colorectal cancer. J. Clin. Oncol. *28*, 1254–1261.

Bellahcène, A., Nokin, M.J., Castronovo, V., and Schalkwijk, C. (2018). Methylglyoxal-derived stress: An emerging biological factor involved in the onset and progression of cancer. Semin. Cancer Biol. *49*, 64–74.

Bray, S.M., Lee, J., Kim, S.T., Hur, J.Y., Ebert, P.J., Calley, J.N., Wulur, I.H., Gopalappa, T., Wong, S.S., Qian, H.R., et al. (2019). Genomic characterization of intrinsic and acquired resistance to cetuximab in colorectal cancer patients. Sci. Rep. *9*, 15365.

Brownlee, M. (2001). Biochemistry and molecular cell biology of diabetic complications. Nature *414*, 813–820.

Castellano, E., and Downward, J. (2011). RAS interaction with PI3K: more than just another effector pathway. Genes Cancer *2*, 261–274.

Chandarlapaty, S., Sawai, A., Scaltriti, M., Rodrik-Outmezguine, V., Grbovic-Huezo, O., Serra, V., Majumder, P.K., Baselga, J., and Rosen, N. (2011). AKT inhibition relieves feedback suppression of receptor tyrosine kinase expression and activity. Cancer Cell *19*, 58–71.

Chiavarina, B., Nokin, M.J., Bellier, J., Durieux, F., Bletard, N., Sherer, F., Lovinfosse, P., Peulen, O., Verset, L., Dehon, R., et al. (2017). Methylglyoxal-mediated stress correlates with high metabolic activity and promotes tumor growth in colorectal cancer. Int. J. Mol. Sci. *18*, 213.

Courtney, R., Ngo, D.C., Malik, N., Ververis, K., Tortorella, S.M., and Karagiannis, T.C. (2015). Cancer metabolism and the Warburg effect: the role of HIF-1 and PI3K. Mol. Biol. Rep. *42*, 841–851.

De Roock, W., Claes, B., Bernasconi, D., De Schutter, J., Biesmans, B., Fountzilas, G., Kalogeras, K.T., Kotoula, V., Papamichael, D., Laurent-Puig, P., et al. (2010). Effects of KRAS, BRAF, NRAS, and PIK3CA mutations on the efficacy of cetuximab plus chemotherapy in chemotherapy-refractory metastatic colorectal cancer: a retrospective consortium analysis. Lancet Oncol. *11*, 753–762.

De Roock, W., De Vriendt, V., Normanno, N., Ciardiello, F., and Tejpar, S. (2011). KRAS, BRAF, PIK3CA, and PTEN mutations: implications for targeted therapies in metastatic colorectal cancer. Lancet Oncol. *12*, 594–603.

Di Nicolantonio, F., Martini, M., Molinari, F., Sartore-Bianchi, A., Arena, S., Saletti, P., De Dosso, S., Mazzucchelli, L., Frattini, M., Siena, S., and Bardelli, A. (2008). Wild-type BRAF is required for response to panitumumab or cetuximab in metastatic colorectal cancer. J. Clin. Oncol. *26*, 5705–5712.

Downward, J. (2003). Targeting RAS signalling pathways in cancer therapy. Nat. Rev. Cancer *3*, 11–22.

Ebi, H., Corcoran, R.B., Singh, A., Chen, Z., Song, Y., Lifshits, E., Ryan, D.P., Meyerhardt, J.A., Benes, C., Settleman, J., et al. (2011). Receptor tyrosine kinases exert dominant control over PI3K signaling in human KRAS mutant colorectal cancers. J. Clin. Invest. *121*, 4311–4321.

Elstrom, R.L., Bauer, D.E., Buzzai, M., Karnauskas, R., Harris, M.H., Plas, D.R., Zhuang, H., Cinalli, R.M., Alavi, A., Rudin, C.M., and Thompson, C.B. (2004). Akt stimulates aerobic glycolysis in cancer cells. Cancer Res. *64*, 3892–3899.

Emi, N., Friedmann, T., and Yee, J.K. (1991). Pseudotype formation of murine leukemia virus with the G protein of vesicular stomatitis virus. J. Virol. *65*, 1202–1207.

Garofalo, M., Iovine, B., Kuryk, L., Capasso, C., Hirvinen, M., Vitale, A., Ylipert-tula, M., Bevilacqua, M.A., and Cerullo, V. (2016). Oncolytic adenovirus loaded with L-carnosine as novel strategy to enhance the antitumor activity. Mol. Cancer Ther. *15*, 651–660.

Guerrero, S., Casanova, I., Farré, L., Mazo, A., Capellà, G., and Mangues, R. (2000). K-ras codon 12 mutation induces higher level of resistance to apoptosis and predisposition to anchorage-independent growth than codon 13 mutation or proto-oncogene overexpression. Cancer Res. *60*, 6750–6756.

Gupta, S., Ramjaun, A.R., Haiko, P., Wang, Y., Warne, P.H., Nicke, B., Nye, E., Stamp, G., Alitalo, K., and Downward, J. (2007). Binding of ras to phosphoinositide 3-kinase p110alpha is required for ras-driven tumorigenesis in mice. Cell *129*, 957–968.

Han, L., Jiang, Y., Han, D., and Tan, W. (2018). Hsp27 regulates epithelial mesenchymal transition, metastasis and proliferation in colorectal carcinoma. Oncol. Lett. *16*, 5309–5316.

Hanahan, D., and Weinberg, R.A. (2011). Hallmarks of cancer: the next generation. Cell *144*, 646–674.

Hardeman, K.N., Peng, C., Paudel, B.B., Meyer, C.T., Luong, T., Tyson, D.R., Young, J.D., Quaranta, V., and Fessel, J.P. (2017). Dependence on glycolysis sensitizes BRAF-mutated melanomas for increased response to targeted BRAF inhibition. Sci. Rep. *7*, 42604.

Hong, D.S., Morris, V.K., El Osta, B., Sorokin, A.V., Janku, F., Fu, S., Overman, M.J., Piha-Paul, S., Subbiah, V., Kee, B., et al. (2016). Phase IB study of vemurafenib in combination with irinotecan and cetuximab in patients with metastatic colorectal cancer with BRAFV600E mutation. Cancer Discov. *6*, 1352–1365.

Hu, Y., Lu, W., Chen, G., Wang, P., Chen, Z., Zhou, Y., Ogasawara, M., Trachootham, D., Feng, L., Pelicano, H., et al. (2012). K-ras(G12V) transformation leads to mitochondrial dysfunction and a metabolic switch from oxidative phosphorylation to glycolysis. Cell Res. *22*, 399–412.

Huang, Q., Ye, J., Huang, Q., Chen, W., Wang, L., Lin, W., Lin, J., and Lin, X. (2010). Heat shock protein 27 is over-expressed in tumor tissues and increased in sera of patients with gastric adenocarcinoma. Clin. Chem. Lab. Med. *48*, 263–269.

Iovine, B., Iannella, M.L., Nocella, F., Pricolo, M.R., and Bevilacqua, M.A. (2012). Carnosine inhibits KRAS-mediated HCT116 proliferation by affecting ATP and ROS production. Cancer Lett. *315*, 122–128.

Jhawer, M., Goel, S., Wilson, A.J., Montagna, C., Ling, Y.H., Byun, D.S., Nasser, S., Arango, D., Shin, J., Klampfer, L., et al. (2008). PIK3CA mutation/PTEN expression status predicts response of colon cancer cells to the epidermal growth factor receptor inhibitor cetuximab. Cancer Res. *68*, 1953–1961.

Kamada, M., So, A., Muramaki, M., Rocchi, P., Beraldi, E., and Gleave, M. (2007). Hsp27 knockdown using nucleotide-based therapies inhibit tumor growth and enhance chemotherapy in human bladder cancer cells. Mol. Cancer Ther. *6*, 299–308.

Kennedy, A.L., Morton, J.P., Manoharan, I., Nelson, D.M., Jamieson, N.B., Pawlikowski, J.S., McBryan, T., Doyle, B., McKay, C., Oien, K.A., et al. (2011). Activation of the PIK3CA/AKT pathway suppresses senescence induced by an activated RAS oncogene to promote tumorigenesis. Mol. Cell *42*, 36–49.

Kovalski, J.R., Bhaduri, A., Zehnder, A.M., Neela, P.H., Che, Y., Wozniak, G.G., and Khavari, P.A. (2019). The functional proximal proteome of oncogenic Ras includes mTORC2. Mol. Cell *73*, 830–844.e12.

Kuramitsu, Y., Wang, Y., Taba, K., Suenaga, S., Ryozawa, S., Kaino, S., Sakaida, I., and Nakamura, K. (2012). Heat-shock protein 27 plays the key role in gemcitabine-resistance of pancreatic cancer cells. Anticancer Res. *32*, 2295–2299.

Lee, J., Park, J.R., Lee, H., Jang, S., Ryu, S.M., Kim, H., Kim, D., Jang, A., and Yang, S.R. (2018). L-carnosine induces apoptosis/cell cycle arrest via suppression of NF-κB/STAT1 pathway in HCT116 colorectal cancer cells. In Vitro Cell. Dev. Biol. Anim. *54*, 505–512.

Li, Y., Dong, Q., and Cui, Y. (2019). Synergistic inhibition of MEK and reciprocal feedback networks for targeted intervention in malignancy. Cancer Biol. Med. *16*, 415–434.

Lièvre, A., Bachet, J.B., Le Corre, D., Boige, V., Landi, B., Emile, J.F., Côté, J.F., Tomasic, G., Penna, C., Ducreux, M., et al. (2006). KRAS mutation status is predictive of response to cetuximab therapy in colorectal cancer. Cancer Res. *66*, 3992–3995.

Lovinfosse, P., Koopmansch, B., Lambert, F., Jodogne, S., Kustermans, G., Hatt, M., Visvikis, D., Seidel, L., Polus, M., Albert, A., et al. (2016). (18)F-FDG PET/CT imaging in rectal cancer: relationship with the RAS mutational status. Br. J. Radiol. *89*, 20160212.

Lu, H., Li, X., Luo, Z., Liu, J., and Fan, Z. (2013). Cetuximab reverses the Warburg effect by inhibiting HIF-1-regulated LDH-A. Mol. Cancer Ther. *12*, 2187–2199.

Luraghi, P., Bigatto, V., Cipriano, E., Reato, G., Orzan, F., Sassi, F., De Bacco, F., Isella, C., Bellomo, S.E., Medico, E., et al. (2018). A molecularly annotated model of patient-derived colon cancer stem-like cells to assess genetic and nongenetic mechanisms of resistance to anti-EGFR therapy. Clin. Cancer Res. *24*, 807–820.

Mackay, G.M., Zheng, L., van den Broek, N.J., and Gottlieb, E. (2015). Analysis of cell metabolism using LC-MS and isotope tracers. Methods Enzymol. *561*, 171–196.

Maessen, D.E., Stehouwer, C.D., and Schalkwijk, C.G. (2015). The role of methylglyoxal and the glyoxalase system in diabetes and other age-related diseases. Clin. Sci. (Lond.) *128*, 839–861.

Mearow, K.M., Dodge, M.E., Rahimtula, M., and Yegappan, C. (2002). Stress-mediated signaling in PC12 cells - the role of the small heat shock protein, Hsp27, and Akt in protecting cells from heat stress and nerve growth factor withdrawal. J. Neurochem. *83*, 452–462.

Melle, C., Ernst, G., Escher, N., Hartmann, D., Schimmel, B., Bleul, A., Thieme, H., Kaufmann, R., Felix, K., Friess, H.M., et al. (2007). Protein profiling of microdissected pancreas carcinoma and identification of HSP27 as a potential serum marker. Clin. Chem. *53*, 629–635.

Mori-Iwamoto, S., Kuramitsu, Y., Ryozawa, S., Mikuria, K., Fujimoto, M., Maehara, S., Maehara, Y., Okita, K., Nakamura, K., and Sakaida, I. (2007). Proteomics finding heat shock protein 27 as a biomarker for resistance of pancreatic cancer cells to gemcitabine. Int. J. Oncol. *31*, 1345–1350.

Nokin, M.J., Durieux, F., Peixoto, P., Chiavarina, B., Peulen, O., Blomme, A., Turtoi, A., Costanza, B., Smargiasso, N., Baiwir, D., et al. (2016). Methylglyoxal, a glycolysis side-product, induces Hsp90 glycation and YAP-mediated tumor growth and metastasis. eLife *5*, e19375.

Nokin, M.J., Durieux, F., Bellier, J., Peulen, O., Uchida, K., Spiegel, D.A., Cochrane, J.R., Hutton, C.A., Castronovo, V., and Bellahcène, A. (2017). Hormetic potential of methylglyoxal, a side-product of glycolysis, in switching tumours from growth to death. Sci. Rep. *7*, 11722.

Nokin, M.J., Bellier, J., Durieux, F., Peulen, O., Rademaker, G., Gabriel, M., Monseur, C., Charloteaux, B., Verbeke, L., van Laere, S., et al. (2019). Methylglyoxal, a glycolysis metabolite, triggers metastasis through MEK/ERK/SMAD1 pathway activation in breast cancer. Breast Cancer Res. *21*, 11.

Oya, T., Hattori, N., Mizuno, Y., Miyata, S., Maeda, S., Osawa, T., and Uchida, K. (1999). Methylglyoxal modification of protein. Chemical and immunochemical characterization of methylglyoxal-arginine adducts. J. Biol. Chem. *274*, 18492–18502.

Oya-Ito, T., Liu, B.F., and Nagaraj, R.H. (2006). Effect of methylglyoxal modification and phosphorylation on the chaperone and anti-apoptotic properties of heat shock protein 27. J. Cell. Biochem. *99*, 279–291.

Oya-Ito, T., Naito, Y., Takagi, T., Handa, O., Matsui, H., Yamada, M., Shima, K., and Yoshikawa, T. (2011). Heat-shock protein 27 (Hsp27) as a target of methylglyoxal in gastrointestinal cancer. Biochim. Biophys. Acta *1812*, 769–781.

Parmenter, T.J., Kleinschmidt, M., Kinross, K.M., Bond, S.T., Li, J., Kaadige, M.R., Rao, A., Sheppard, K.E., Hugo, W., Pupo, G.M., et al. (2014). Response of BRAF-mutant melanoma to BRAF inhibition is mediated by a network of transcriptional regulators of glycolysis. Cancer Discov. *4*, 423–433.

Parseghian, C.M., Napolitano, S., Loree, J.M., and Kopetz, S. (2019). Mechanisms of innate and acquired resistance to anti-EGFR therapy: a review of current knowledge with a focus on rechallenge therapies. Clin. Cancer Res. *25*, 6899–6908.

Parsons, D.W., Wang, T.L., Samuels, Y., Bardelli, A., Cummins, J.M., DeLong, L., Silliman, N., Ptak, J., Szabo, S., Willson, J.K., et al. (2005). Colorectal cancer: mutations in a signalling pathway. Nature *436*, 792.

Rabbani, N., and Thornalley, P.J. (2012a). Glycation research in amino acids: a place to call home. Amino Acids *42*, 1087–1096.

Rabbani, N., and Thornalley, P.J. (2012b). Methylglyoxal, glyoxalase 1 and the dicarbonyl proteome. Amino Acids *42*, 1133–1142.

Racker, E., Resnick, R.J., and Feldman, R. (1985). Glycolysis and methylaminoisobutyrate uptake in rat-1 cells transfected with ras or myc oncogenes. Proc. Natl. Acad. Sci. USA *82*, 3535–3538.

Rademaker, G., Hennequière, V., Brohée, L., Nokin, M.J., Lovinfosse, P., Durieux, F., Gofflot, S., Bellier, J., Costanza, B., Herfs, M., et al. (2018). Myoferlin controls mitochondrial structure and activity in pancreatic ductal adenocarcinoma, and affects tumor aggressiveness. Oncogene *37*, 4398–4412.

Rane, M.J., Pan, Y., Singh, S., Powell, D.W., Wu, R., Cummins, T., Chen, Q., McLeish, K.R., and Klein, J.B. (2003). Heat shock protein 27 controls apoptosis by regulating Akt activation. J. Biol. Chem. *278*, 27828–27835.

Rath, N., Munro, J., Cutiongco, M.F., Jagiełło, A., Gadegaard, N., McGarry, L., Unbekandt, M., Michalopoulou, E., Kamphorst, J.J., Sumpton, D., et al. (2018). Rho kinase inhibition by AT13148 blocks pancreatic ductal adenocarcinoma invasion and tumor growth. Cancer Res. *78*, 3321–3336.

Rathmell, J.C., Fox, C.J., Plas, D.R., Hammerman, P.S., Cinalli, R.M., and Thompson, C.B. (2003). Akt-directed glucose metabolism can prevent Bax conformation change and promote growth factor-independent survival. Mol. Cell. Biol. *23*, 7315–7328.

Richard, J.P. (1993). Mechanism for the formation of methylglyoxal from triosephosphates. Biochem. Soc. Trans. *21*, 549–553.

Robey, R.B., and Hay, N. (2009). Is Akt the "Warburg kinase"?-Akt-energy metabolism interactions and oncogenesis. Semin. Cancer Biol. *19*, 25–31.

Rodriguez-Viciana, P., Warne, P.H., Dhand, R., Vanhaesebroeck, B., Gout, I., Fry, M.J., Waterfield, M.D., and Downward, J. (1994). Phosphatidylinositol-3-OH kinase as a direct target of Ras. Nature *370*, 527–532.

Sakamoto, H., Mashima, T., Yamamoto, K., and Tsuruo, T. (2002). Modulation of heat-shock protein 27 (Hsp27) anti-apoptotic activity by methylglyoxal modification. J. Biol. Chem. *277*, 45770–45775.

Salgado, R., Moore, H., Martens, J.W.M., Lively, T., Malik, S., McDermott, U., Michiels, S., Moscow, J.A., Tejpar, S., McKee, T., and Lacombe, D.; IBCD-Faculty (2018). Steps forward for cancer precision medicine. Nat. Rev. Drug Discov. *17*, 1–2.

Sarbassov, D.D., Guertin, D.A., Ali, S.M., and Sabatini, D.M. (2005). Phosphorylation and regulation of Akt/PKB by the rictor-mTOR complex. Science *307*, 1098–1101.

Sartore-Bianchi, A., Martini, M., Molinari, F., Veronese, S., Nichelatti, M., Artale, S., Di Nicolantonio, F., Saletti, P., De Dosso, S., Mazzucchelli, L., et al. (2009). PIK3CA mutations in colorectal cancer are associated with clinical resistance to EGFR-targeted monoclonal antibodies. Cancer Res. *69*, 1851–1857.

Scheijen, J.L., and Schalkwijk, C.G. (2014). Quantification of glyoxal, methylglyoxal and 3-deoxyglucosone in blood and plasma by ultra performance liquid chromatography tandem mass spectrometry: evaluation of blood specimen. Clin. Chem. Lab. Med. *52*, 85–91.

Schneider, C.A., Rasband, W.S., and Eliceiri, K.W. (2012). NIH Image to ImageJ: 25 years of image analysis. Nat. Methods *9*, 671–675.

Sullivan, L.B., Gui, D.Y., and Vander Heiden, M.G. (2016). Altered metabolite levels in cancer: implications for tumour biology and cancer therapy. Nat. Rev. Cancer *16*, 680–693.

Thornalley, P.J., Westwood, M., Lo, T.W., and McLellan, A.C. (1995). Formation of methylglyoxal-modified proteins in vitro and in vivo and their involvement in AGE-related processes. Contrib. Nephrol. *112*, 24–31.

Troiani, T., Napolitano, S., Della Corte, C.M., Martini, G., Martinelli, E., Morgillo, F., and Ciardiello, F. (2016). Therapeutic value of EGFR inhibition in CRC and NSCLC: 15 years of clinical evidence. ESMO Open *1*, e000088.

Turke, A.B., Song, Y., Costa, C., Cook, R., Arteaga, C.L., Asara, J.M., and Engelman, J.A. (2012). MEK inhibition leads to PI3K/AKT activation by relieving a negative feedback on ERBB receptors. Cancer Res. *72*, 3228–3237.

Van Emburgh, B.O., Sartore-Bianchi, A., Di Nicolantonio, F., Siena, S., and Bardelli, A. (2014). Acquired resistance to EGFR-targeted therapies in colorectal cancer. Mol. Oncol. *8*, 1084–1094.

van Heijst, J.W., Niessen, H.W., Musters, R.J., van Hinsbergh, V.W., Hoekman, K., and Schalkwijk, C.G. (2006). Argpyrimidine-modified Heat shock protein 27 in human non-small cell lung cancer: a possible mechanism for evasion of apoptosis. Cancer Lett. *241*, 309–319.

Vander Heiden, M.G., and DeBerardinis, R.J. (2017). Understanding the intersections between metabolism and cancer biology. Cell *168*, 657–669.

Vander Heiden, M.G., Cantley, L.C., and Thompson, C.B. (2009). Understanding the Warburg effect: the metabolic requirements of cell proliferation. Science *324*, 1029–1033.

Vitiello, P.P., Cardone, C., Martini, G., Ciardiello, D., Belli, V., Matrone, N., Barra, G., Napolitano, S., Della Corte, C., Turano, M., et al. (2019). Receptor tyrosine kinase-dependent PI3K activation is an escape mechanism to vertical suppression of the EGFR/RAS/MAPK pathway in KRAS-mutated human colorectal cancer cell lines. J. Exp. Clin. Cancer Res. *38*, 41.

Waltregny, D., Bellahcène, A., Van Riet, I., Fisher, L.W., Young, M., Fernandez, P., Dewé, W., de Leval, J., and Castronovo, V. (1998). Prognostic value of bone sialoprotein expression in clinically localized human prostate cancer. J. Natl. Cancer Inst. *90*, 1000–1008.

Wang, T., Douglass, E.F., Jr., Fitzgerald, K.J., and Spiegel, D.A. (2013). A "turn-on" fluorescent sensor for methylglyoxal. J. Am. Chem. Soc. *135*, 12429–12433.

Yu, Z., Zhi, J., Peng, X., Zhong, X., and Xu, A. (2010). Clinical significance of HSP27 expression in colorectal cancer. Mol. Med. Rep. *3*, 953–958.

Yun, J., Rago, C., Cheong, I., Pagliarini, R., Angenendt, P., Rajagopalan, H., Schmidt, K., Willson, J.K., Markowitz, S., Zhou, S., et al. (2009). Glucose deprivation contributes to the development of KRAS pathway mutations in tumor cells. Science *325*, 1555–1559.

STAR★METHODS

KEY RESOURCES TABLE

REAGENT or RESOURCE	SOURCE	IDENTIFIER
Antibodies		
Argpyrimidine	(Oya et al., 1999)	Cat# mAb6B
β-actin	Sigma-Aldrich	Cat# A5441; RRID: AB_476744
Glyoxalase 1	BioMAC	Cat# 02-14
MG-Hs (3D11)	Cell Biolabs	Cat# STA-011
P-AKT	Cell Signaling	Cat# 4060; RRID: AB_2315049
AKT	Cell Signaling	Cat# 9272; RRID: AB_329827
P-PI3K	Cell Signaling	Cat# 4228; RRID: AB_659940
PI3K	Cell Signaling	Cat# 4257
GLUT1	Cell Signaling	Cat# 12939; RRID: AB_2687899
P-PDH	Abcam	Cat# 92696; RRID: AB_10711672
PDH	Abcam	Cat# 168379
P-PKM2	Cell Signaling	Cat# 3827; RRID: AB_1950369
PKM2	Cell signaling	Cat# 4053; RRID: AB_1904096
P-P70S6K	Cell signaling	Cat# 2708; RRID: AB_390722
P-GSK3beta	Cell signaling	Cat# 9331; RRID: AB_329830
GSK3beta	BD Biosciences	Cat# 610202; RRID: AB_397601
Hsp27	Enzo Life Sciences	Cat# ADI-SPA-803-D; RRID: AB_10615084
Cleaved caspase 3	Cell Signaling	Cat# 9664; RRID: AB_2070042
Cleaved PARP	Cell Signaling	Cat# 5625; RRID: AB_10699459
HKII	Cell Signaling	Cat# 2867; RRID: AB_2232946
PFKFB3	Cell Signaling	Cat# 13123; RRID: AB_2617178
Rictor	Cell Signaling	Cat# 2114; RRID: AB_2179963
mTOR	Cell Signaling	Cat# 2983; RRID: AB_2105622
Hsc70	Santa Cruz	Cat# Sc-7298; RRID: AB_627761
Bacterial and Virus Strains		
pSPAX2	Addgene	#12260
VSV-G encoding vector	Emi et al., 1991	N/A
GLO1#1 shRNA plasmid	Sigma-Aldrich	TRCN0000118627
GLO1#4 shRNA plasmid	Sigma-Aldrich	TRCN0000118631
Non-target shRNA plasmid	Sigma-Aldrich	SHC005
Chemicals, Peptides, and Recombinant Proteins		
L-carnosine	Sigma-Aldrich	Cat# C-9625
Aminoguanidine	Sigma-Aldrich	Cat# 396494
Deoxyglucose	Sigma-Aldrich	Cat# D-8375
Methylglyoxal	Sigma-Aldrich	Cat# M-0252
Cycloheximide	Sigma-Aldrich	Cat# C-7698
Human recombinant Hsp27	Enzo Life Sciences	Cat# ADI-SPP-715-D
Torin 1	Selleckchem	Cat# S2827
SC79	Selleckchem	Cat# S7863
LY294002	Selleckchem	Cat# S1105
BYL719	Selleckchem	Cat# S2814
MK2206	Selleckchem	Cat# S1078
Rapamycin	Calbiochem	Cat# 553210
Cetuximab	Merck	C225

(*Continued on next page*)

Continued		
REAGENT or RESOURCE	SOURCE	IDENTIFIER
NAD+	Sigma-Aldrich	Cat# N7004
D-Lactate Dehydrogenase	Sigma-Aldrich	Cat# L3888
Glutathione reduced (GSH)	Sigma-Aldrich	Cat# G4251
Bisbenzimide	Sigma-Aldrich	Cat# 33258
Seahorse XF Base Medium	Agilent	Cat# 102353-100
Oligomycin	Sigma-Aldrich	Cat# O4876
Lipofectamine 2000	Thermo Fisher	Cat# 11668-019
Methyl diaminobenzene-BODIPY (MBo)	Wang et al., 2013	N/A
Critical Commercial Assays		
Pierce BCA Protein Assay Kit	Pierce	Cat# PI-23225
Vectastain ABC Kit	Vector Laboratories	Cat# PK-6100
FITC-Annexin V apoptosis Detection Kit I	BD Biosciences	Cat# 556547
BioPORTER Protein Delivery Kit	Sigma-Aldrich	Cat# BPQ24
qPCR Lentivirus Titration Kit	ABM	Cat# LV900
Experimental Models: Cell Lines		
Isogenic SW48 ($KRAS^{WT}$)	Horizon Discovery	Cat# HD PAR-006
Isogenic SW48 ($KRAS^{G12V}$)	Horizon Discovery	Cat#: HD 103-007
Isogenic LIM1215 ($KRAS^{WT}$)	Horizon Discovery	Cat# HD PAR-108
Isogenic LIM1215 ($KRAS^{G12V}$)	Horizon Discovery	Cat# HD 116-006
Experimental Models: Organisms/Strains		
NOD-SCID – Males (6-8 weeks old)	Animal facility University of Liège	N/A
Oligonucleotides		
GLO1#1 siRNA: 5′-CUUGGCUUAUGAGGAUAAAUU-3′	Eurogentec	N/A
GLO1#2 siRNA: 5′-GAUGGCUACUGGAUUGAAAUU-3′	Eurogentec	N/A
Hsp27#1 siRNA: 5′-GUCUCAUCGGAUUUUGCAGC-3′	Eurogentec	N/A
Hsp27#2 siRNA: 5′-AAGUCUAUCGGAUUUUGCAGC-3′	Eurogentec	N/A
Irrelevant siRNA: 5′-CUUACGCUGAGUACUUCGA-3′	Eurogentec	N/A
Software and Algorithms		
GraphPad Prism 6	Graphpad Software	N/A
Fiji-ImageJ	https://imagej.net/Fiji	N/A
IncuCyte S3 (V2019A)	Essen Bioscience	N/A

LEAD CONTACT AND MATERIALS AVAILABILITY

Further information and requests for resources and reagents should be directed to and will be fulfilled by the Lead Contact, Akeila Bellahcène (a.bellahcene@uliege.be). This study did not generate new unique reagents.

EXPERIMENTAL MODEL AND SUBJECT DETAILS

Clinical tumor samples

Retrospective series of CRC samples comprising colon and rectum primary tumors were provided by the Biobank of the University Hospital of Liège (Liège University, Belgium). The use of human sample collections has been approved by the institutional ethics committee of the University of Liège (ethics committee approval number 2013/302). The cohort of 48 colon cancer patients consisted of 22 males and 26 females diagnosed between October 2006 and January 2018. The median age was 66 years (range: 33–86 years). Sex, age, pTNM staging and grade were retrieved from medical reports (Table S1). KRAS, NRAS, BRAF, PTEN and PIK3CA mutational status of CRC tumors was assessed as described below and summarized in Table S1. The cohort of 84 rectum cancer

patients consisted of 51 males and 33 females diagnosed between September 2009 and December 2015. The median age was 68 years (range: 39–92 years). Sex, age, pTNM staging and grade were retrieved from medical reports and presented in Table S2. For TNM prognostic stage determination, we referred to the 7th edition of the AJCC-UICC (the American Joint Committee on Cancer and Union Internationale Contre le Cancer) that also includes grade.

Cell lines

Isogenic human CRC cell lines SW48 and LIM1215 were purchased from Horizon Discovery. The clones used were heterozygous knock-in (G12V/+) of KRAS activating mutation $KRAS^{G12V}$ (SW48 cat. no. HD 103-007 lot 00053 and LIM1215 cat. no. HD 116-006 lot 2874) and homozygous wild-type KRAS expressing cells (SW48 cat. no. HD PAR-006 lot 11916 and LIM1215 cat. no. HD PAR-108 lot 2706). SW48 isogenic cell lines were cultured in RPMI medium (Lonza) containing 10% fetal bovine serum (FBS, ThermoFisher Scientific) and 4.5 g/L of glucose. LIM1215 isogenic cell lines were cultivated in RPMI medium (Lonza) containing 10% fetal bovine serum (FBS, ThermoFisher Scientific), insulin (1 μg/mL), hydrocortisone (1 μg/mL) and 1 g/L of glucose. SW480, Lovo, HCT116, LS174, HT29 human CRC cell lines, all purchased from American Type Culture Collection (ATCC), were cultured in DMEM medium containing 10% FBS and 4.5 g/L of glucose. All cell lines were authenticated by STR profiling at Leibniz-Institute DSMZ (Braunschweig) and were regularly checked for mycoplasma contamination using MycoAlert mycoplasma detection kit (Lonza).

Mouse xenografts

All animal experimental procedures were performed according to the Federation of European Laboratory Animal Sciences Associations (FELASA) and were reviewed and approved by the Institutional Animal Care and Ethics Committee of the University of Liege (ethics committee approval number 17-1913). Animals were housed in the GIGA-accredited animal facility (University of Liege) under standard conditions (12 hr light/dark cycle, light on at 7 a.m., food and water provided *ad libitum*). SW48 $KRAS^{WT}$ and $KRAS^{G12V}$ cells and HCT116 (3×10^6 cells/mouse) were suspended in FBS-free culture medium. LIM1215 $KRAS^{G12V}$ cells ($2{,}5 \times 10^6$ cells/mouse) were suspended in FBS-free culture medium with matrigel (1:1 ratio). Cell suspensions were injected subcutaneously into the right posterior flanks of 7-week-old immunodeficient NOD-SCID male mice (number of mice/group is as indicated in figure legend). Tumor volume was monitored three times per week using caliper and was calculated by the modified ellipsoidal formula (tumor volume = 1/2 (length × $width^2$). When tumors reached a volume of approximately 0.2 cm^3, mice received intra-peritoneal injections of carnosine and/or cetuximab. Mice received carnosine three times per week (100 mg/kg/injection) and/or cetuximab twice a week (0.5 mg/injection). After 7-8 carnosine injections, mice were euthanized and tumors were collected. Tumors were fixed and embedded in paraffin for immunohistochemistry.

METHOD DETAILS

Mutational status analysis using NGS

DNA was extracted from FFPE human CRC tumor samples. The regions of interest and detailed below were amplified using a laboratory developed multiplex PCR using QIAGEN multiplex PCR plus kit (QIAGEN). Molecular barcoding was performed with 'drMID DX 1-48 for Illumina NGS system' or 'drMID DX 49-96 for Illumina NGS system' (Agilent, USA) according to the manufacturer's protocol. PCR products obtained from each sample were pooled and purified using Agencourt AMPure XP beads (Beckman Coulter, USA). Each patient library was then quantified using Quanti-it Picogreen dsDNA Assay Kit (Fisher Scientific, USA) and the Fluostar Optima System (BMG Labtech, Germany). Equimolar amounts of each patient PCR products were pooled to obtain the final library. The library was then quantified and denatured according to the standard Illumina's MiSeq protocol. Sequencing was performed with a MiSeq v3 cartridge with 500 cycles (Illumina, USA). Alignment of the fastq files and variant calling were made using SeqNext Version 4.1.1 build 511 (JSI medical systems, Germany). Regions of interest: *KRAS* [exons 2, 3 and 4 (full)], *NRAS* [exons 2, 3 and 4 (full)], *BRAF* [exons 11 and 15 (full)], *PIK3CA* [hotspots in exon 9 and 20 (codons 542, 545 and 1047 covered)] and *PTEN* [exons 5 and 7 (full)].

Immunohistochemistry (IHC)

Formalin-fixed paraffin embedded sections were deparaffinized in xylene and rehydrated. Sections were treated with 3% hydrogen peroxide in methanol for 30 min to block endogenous peroxidase activity and washed in PBS for 20 min. Antigen retrieval was performed in sodium citrate buffer (10 mM) pH 6 at 95°C for 40 min. To block non-specific serum-binding sites, sections were then incubated with 1.5% normal serum (Vector Laboratories) for 30 min. Next, they were incubated with mouse anti-Argpyrimidine (mAb6B, 1:5000), rabbit anti-Hsp27 (Enzo Life Sciences, 1:100 dilution) rabbit anti-P-AKT (Cell signaling, 1:100 dilution) and mouse anti-Ki67 (Dako, 1:100 dilution) antibodies overnight at 4°C. Antibody binding was detected using anti-mouse or anti-rabbit biotinylated secondary antibody (Vector Laboratories) for 30 min at room temperature. Sections were then incubated with the avidin-biotin-peroxidase complex (Vectastain ABC Kit) for 30 min followed by immunoreactivity revelation with 3,3′ diaminobenzidine tetrachloride. Slides were finally counterstained with hematoxylin, dehydrated and mounted with DPX (Sigma-Aldrich). Tissue sections incubated without primary antibody showed no detectable immunoreactivity.

Seahorse analysis

Extracellular acidification rate (ECAR) of cells was determined using Seahorse XFp extracellular flux analyzer (Agilent) according to manufacturer's recommendations and as we described previously (Nokin et al., 2017; Rademaker et al., 2018). SW48 and LIM1215

cells were seeded (30,000 cells/well) in XFp mini-plates (Agilent) and allowed to attach overnight. Cells were kept at 37°C for 1 hr in unbuffered serum-free DMEM (Basal DMEM, Agilent) containing glutamine (2 mM), pH 7.4 before the measurements. During the assay, cells were successively stressed with glucose (20 mM), oligomycin (1 μM) and 2-deoxyglucose (50 mM). All results were normalized according to the cell number evaluated by Hoechst (2 μg/mL) incorporation after cold methanol/acetone fixation. Representative results of at least two independent experiments are shown.

Metabolomics

Extraction of polar metabolites was performed after 48 hours of cell culture (steady state). For tracing experiments, cells were further incubated in glucose-free RPMI (GIBCO, Thermo Fisher Scientific) supplemented with 10% FBS and 10 mM ^{13}C-glucose (CLM-1396, Cambridge Isotopes Laboratories). Briefly, cells were washed with ice-cold PBS and quickly incubated in ice-cold extraction buffer (50% Methanol - 30% Acetonitrile - 20% H_2O) for 5 minutes under agitation. Supernatant was collected, mixed for 10 minutes and centrifuged at 16.000 x g to remove cell debris. All the steps were performed at 4°C. Finally, supernatant was transferred to glass HPLC vials (Thermo Fisher Scientific) and analyzed as previously described (Mackay et al., 2015; Rath et al., 2018) using a Q Exactive Orbitrap mass spectrometer (Thermo Fisher Scientific) coupled with a Thermo Ultimate 3000 HPLC system. The HPLC setup consisted of a ZIC-pHILIC column (SeQuant, 150 × 2.1mm, 5μm, Merck KGaA, Darmstadt, Germany), with a ZIC-pHILIC guard column (SeQuant, 20 × 2.1mm) and an initial mobile phase of 20% 20 mM ammonium carbonate, pH 9.2, and 80% acetonitrile. 5 μl of samples were injected and metabolites were separated over a 15 minute mobile phase gradient, decreasing the acetonitrile content to 20%, at a flow rate of 200 μL/min and a column temperature of 45°C. The total analysis time was 25 minutes. All metabolites were detected across a mass range of 75-1000 m/z using the Q Exactive mass spectrometer at a resolution of 35,000 (at 200 m/z), with electrospray (ESI) ionisation and polarity switching to enable both positive and negative ions to be determined in the same run. Lock masses were used and the mass accuracy obtained for all metabolites was below 5ppm. Data were acquired with Thermo Xcalibur software. Metabolites identification was performed using Thermo TraceFinder 4.0 software (Thermo Fisher Scientific). Commercial standards of all metabolites detected have been analyzed previously on this LC-MS system with the pHILIC column. Peak areas for each metabolite were normalized to protein content.

MGO measurement

Cells were either treated with carnosine (100 mM, 48 hr), aminoguanidine (10 mM, 48 hr) or with siRNA directed against GLO1. Forty-eight hours culture media were collected and centrifuged. Supernatants were snap-frozen and kept at −80°C until analysis. Levels of MGO were determined in conditioned medium by derivatization with o-phenylenediamine (oPD) and analyzed by stable isotope dilution ultra-performance liquid chromatography tandem mass spectrometry (UPLC-MS/MS) as described previously (Scheijen and Schalkwijk, 2014). Briefly, 30 μl of culture medium were mixed with 90 μL oPD (10 mg oPD in 10 mL of 1.6 mol/l perchloric acid) in an Eppendorf cup. After an overnight reaction at room temperature and shielded from light, 10 μL of internal standard solution was added. Samples were mixed and subsequently centrifuged for 20 min at 21,000 g at a temperature of 4°C; 10 μL were injected for UPLC/MS/MS analysis. MGO concentrations were normalized to the corresponding cell numbers. Data are presented as mean ± SEM of three biological replicates.

For MGO tracing, cells were incubated with ^{13}C-glucose (CLM-1396, Cambridge Isotopes Laboratories) for 48 hours. Both unlabeled MGO and labeled MGO were derivatized and processed for LC/MS/MS on cell pellets and conditioned media of SW48 and LIM1215 cells as described above. Data are presented as chromatograms of one representative measure from 3 biological replicates.

Cellular MGO quantification

Methyl diaminobenzene-BODIPY (MBo) was used to detect endogenous MGO as we described previously (Nokin et al., 2016). Cells were treated with 5 μM MBo in complete medium. After 1 hr, cells were washed with PBS and incubated during 3 hr in the presence of the indicated concentrations of MGO or 48 hr after GLO1 silencing using siRNAs. The presence of significant formaldehyde contamination (< 3%) in methylglyoxal was excluded (lot: BCBQ9416V) by NMR analysis. Cells were trypsinized and analyzed by flow cytometry (BD Biosciences FACSCalibur). Data are presented as mean ± SEM of three biological replicates.

Western blot analysis

Cell and tissue proteins were extracted in SDS 1% buffer containing protease and phosphatase inhibitors (Roche). Protein concentrations were determined using the bicinchoninic acid (BCA) assay (Pierce). Twenty μg of proteins were separated by 7.5 to 12.5% sodium dodecyl sulfate polyacrylamide gel electrophoresis (SDS-PAGE) and transferred to a PVDF membrane. Membranes were blocked in TBS-Tween 0.1% containing 5% non fat dried milk (Bio-Rad) and were incubated overnight at 4°C with the indicated primary antibodies and listed in the Key Resources Table. Membranes were exposed to appropriate horseradish peroxidase-conjugated secondary antibody anti-mouse (Dako, 1:3000 dilution) or anti-rabbit (Invitrogen, 1:3000 dilution) at RT for 1 hr. The immunoreactive bands were visualized using Enhanced Chemiluminescence Western Blotting substrate (Pierce). Immunoblots were quantified by densitometric analysis and normalized for β-actin or Hsc70 using ImageJ software (Schneider et al., 2012).

D-lactate dosage

D-lactate concentrations were assessed in 48 hr cell culture media as described previously (Nokin et al., 2017). Briefly, conditioned medium was incubated in presence of NAD+, hydrazine an D-lactate dehydrogenase enzyme (Sigma-Aldrich). D-Lactate concentration

was determined by comparing NADH formation measured at 320 nm to the absorbance of a calibration curve. D-lactate concentrations were normalized per million cells and presented as mean ± SEM of three biological replicates.

GLO1 activity

GLO1 activity was assessed as described previously (Nokin et al., 2017). Briefly, proteins were extracted with RIPA buffer, quantified and mixed with a pre-incubated (15 min at 25°C) equimolar (1 mM) mixture of MGO and GSH (Sigma-Aldrich) in 50 mM sodium phosphate buffer, pH 6.8. S-D-lactoylglutathione formation was followed spectrophotometrically by the increase of absorbance at 240 nm. GLO1 activity is expressed as arbitrary units (A.U.) of enzyme per mg of proteins. Data are presented as mean ± SEM of three biological replicates.

Determination of half-maximal inhibitory concentrations 50 (IC_{50})

Cells were plated in 24-well plate and treated for 24 hr with increasing concentrations of LY294002 (1 to 150 μM), BYL719 (1 to 100 μM), MK2206 (1 to 50 μM) or carnosine (1 to 500 mM). Cells were then washed, lysed by sonication and their DNA content was assessed spectrophotometrically using bisbenzimide (Sigma-Aldrich) incorporation. IC_{50} values represent the concentration of drug able to decrease by half the quantity of DNA.

Apoptosis assay

Apoptosis was assessed by using FITC-Annexin V apoptosis Detection Kit I (BD Biosciences) according to manufacturer's instructions. Flow cytometry data were acquired on a FACSCalibur II and data were analyzed using CellQuest software (BD Biosciences). Data are presented as mean ± SEM of at least three biological replicates.

Immunoprecipitation

Proteins were extracted in Tris-HCl pH 8 (20 mM), NaCl (137 mM), NP-40 1%, EDTA (2 mM) in presence of protease inhibitors and were incubated under rotation at 4°C during 30 min. Cell lysates were centrifuged at 14,000 g for 15 min at 4°C. Five hundred μg of proteins were incubated overnight with 5 μg of anti-argpyrimidine (mAb6B), 5 μg of anti-Hsp27 (Enzo Life Sciences) or the corresponding control anti-mouse and anti-rabbit IgG (Zymed Laboratories) antibodies as indicated. The mixtures were then incubated during 2 hr with protein G magnetic beads at 4°C. After several washes, proteins were eluted and analyzed by western blot. Representative western blots of three independent immunoprecipitation experiments are shown.

BioPORTER assay

Recombinant human Hsp27 (rhHsp27) was modified with MGO (500 μM) in PBS (100 mM) pH 7.4 at 37°C during 24 hr. Native rhHsp27 or MGO-modified rhHsp27 (MGO-rhHsp27) were incubated in presence of BioPORTER reagent according to the manufacturer's instructions (Sigma-Aldrich). Briefly, 75 μl of PBS containing 7.5 μg of rhHsp27 or MGO-rhHsp27 were added to hydrate one QuikEase tube containing the dried BioPORTER reagent. The mixture was gently incubated at room temperature during 5 min. Final volume of the mixture was next brought to 500 μL with serum-free medium. After washing cells with serum-free medium, BioPORTER/protein mix was transferred onto cells for 2 hr at 37°C.

siRNA and shRNA transfections

Lipofectamine-mediated transfection was performed using 20 nM of each small interfering RNA (siRNA) as we described previously (Nokin et al., 2016). Lentiviral vectors (rLV) were generated at the GIGA Viral Vectors platform (University of Liege). Briefly, Lenti-X 293T cells (Clontech, Montain View, CA, USA) were co-transfected with a pSPAX2 (Addgene plasmid #12260) and a VSV-G encoding vector (Emi et al., 1991) along with shRNAs transfer lentiviral plasmids. Forty-eight, 72 and 96 hr post-transfection, viral supernatants were collected, filtrated and concentrated 100x by ultracentrifugation. The lentiviral vectors were then titrated with qPCR Lentivirus Titration Kit (ABM, Richmond, Canada). LIM1215 cells were stably transduced with shGLO1#1, shGLO1#4 and shNT and selected with puromycin (0.5 mg/ml, Sigma-Aldrich). siRNAs and shRNAs sequences are given in the Key Resources Table.

Protein stability

Cells were seeded in 6-well plates overnight and changed to fresh medium supplemented with 10 μg/ml cycloheximide. Cell lysates were prepared after culturing cells for the indicated lengths of time and total Hsp27, MGO-Hsp27, P-AKT, AKT and β-actin protein levels were assessed using immunobloting as described above. A representative western blot of three independent experiments is shown. Data were analyzed by nonlinear regression, and protein half-life was determined from first-order decay constants (k) obtained using PRISM software program (GraphPad).

Clonogenic assay

Cells were seeded (2,000 cells/well) in 6 well-plates and allowed to attach overnight. Cells were kept in the same culture medium and treated once at the indicated concentrations of carnosine. Fourteen days after cell plating, the cells were stained with 0.5% crystal violet and 20% methanol for 5 minutes. Plates were rinsed with water and dried at room temperature. Aggregates of 30 cells or more

were considered as colonies and counted using ImageJ software (Schneider et al., 2012). Data are presented as mean ± SEM of two independent experiments.

Real-time proliferation assay

GLO1 stably depleted LIM1215 cells were seeded in triplicate into 96-well plate (20,000 cells/well). After overnight incubation, cells were treated with increasing concentrations of cetuximab (0-1500 μg/ml) and the plate was inserted into the IncuCyte S3 Live-Cell Analysis System for real-time imaging. Phase-contrast images were automatically acquired using a 10x objective lens (four images per well) at 4 hr intervals during 72 hr. The IncuCyte Analyzer provides real-time cellular confluence data based on segmentation of high-definition phase–contrast images. Cell proliferation is expressed as an increase in percentage of confluence relative to the confluence quantified at the initial time of the experiment (4 hr). Cetuximab IC_{50} values were calculated based on IncuCyte confluency data and represent the concentrations leading to a 50% decrease of relative confluency after 24 hr of treatment. IncuCyte assays were performed on 3 biological replicates.

QUANTIFICATION AND STATISTICAL ANALYSIS

Evaluation of immunohistochemical staining

The immunostaining was assessed and scored by two independent examiners. The scoring of argpyrimidines, Hsp27 and P-AKT was assessed according to the intensity of the staining as 0+ (negative) 1+ (low), 2+ (medium) and 3+ (high) and the extension of the staining as 0+ (negative), 1+ (10%–33%), 2+ (34%–66%) and 3+ (67%–100%). When the tumors showed some heterogeneity in the intensity of the staining, the scoring of the staining intensity was assessed according to the staining of the most positive tumor cells, when their estimated percentage represented at least 30% of the total positive tumor cell area. The results obtained with the two scales were multiplied together, yielding a single scale with steps of 0, 1+, 2+, 3+, 4+, 6+, and 9+ (Waltregny et al., 1998). Final IHC scores are shown as low (0+, 1+, 2+ and 3+) and high (4+, 6 and 9+). Ki67 immunostaining was evaluated as the percentage of positive nuclei present in the whole sections as we described previously (Nokin et al., 2017). Low proliferative rate corresponds to tumors presenting $\leq$ 30% of positive nuclei and high proliferative rate to tumors presenting > 30% of positive nuclei.

Statistical analysis

Statistical analysis was performed using GraphPad Prism (Graphpad software, San Diego, CA). Technical and biological replicates were performed as detailed in figure legends and material and methods sections. Results were reported as mean with standard deviation (SD) or standard error of mean (SEM) as indicated in figure legends. Two group comparisons were performed using unpaired Student's t test with or without Welch's correction according to homoscedasticity. When an experiment required comparisons between more than two groups, we performed one-way or two-way ANOVA depending on the number of grouping factors. Dunnet's or Bonferroni's test were applied for simple or multiple comparisons, respectively. In all cases, a bilateral $p < 0.05$ was considered as statistically significant with a 95% confidence interval.

DATA AND CODE AVAILABILITY

This study did not generate any unique datasets or code.